Structures 82 (2025) 110600

Contents lists available at ScienceDirect

Structures

journal homepage: www.elsevier.com/locate/istruc

Efficient simulation of the soil–structure interaction on the dynamic response of a portal frame railway bridge

J. Chordà-Monsonís [a,*], J.C. Sánchez-Quesada [a], E. Moliner [a], A. Romero [b], P. Galvín [b,c], M.D. Martínez-Rodrigo [a]

[a] Universitat Jaume I, Department of Mechanical Engineering and Construction, Avda. Sos Baynat S/N, ES-12071 Castellón de la Plana, Spain
[b] Escuela Técnica Superior de Ingeniería, Universidad de Sevilla, Camino de los Descubrimientos S/N, ES-41092 Sevilla, Spain
[c] ENGREEN, Laboratory of Engineering for Energy and Environmental Sustainability, Universidad de Sevilla, Camino de los Descubrimientos S/N, ES-41092 Sevilla, Spain

ARTICLE INFO

Keywords:
Underpass
Vibration
Acceleration
Experimental measurements
Ballasted track

ABSTRACT

The dynamic response of railway bridges can be highly influenced by the effect of soil–structure interaction. This occurs as the soil dissipates energy and modifies the flexibility of the bridge supports, which impacts the modal parameters of the structure and its response to passing trains. In the case of partially-buried structures such as portal frames, this interaction mechanism is of particular relevance. However, simulating the soil effect is complex, and may require an elevated computational effort. Under these conditions, obtaining accurate predictions of the bridge dynamic behaviour becomes challenging. For this reason, the interplay between the bridge and the soil is usually disregarded. To address this limitation, a numerical approach devoted to implement soil–structure interaction with reduced computational cost is presented in this contribution. The method is based on a substructuring scheme, and considers two numerical models: (i) a full three-dimensional finite-element interaction model, including the track, the bridge, and the surrounding soil, and (ii) a simplified version of it, in which the soil is substituted by a series of linear spring-dampers. The first model is used to derive frequency-dependent dynamic stiffness functions that describe the mechanical coupling between the bridge and the ground. Then, these functions are used to calibrate the spring-damper elements representing the soil in the subsequent simplified model, and the dynamic problem is solved by complex modal superposition. The suitability of the proposed methodology is evaluated through its application to an existing portal frame railway bridge. The effect of other relevant aspects on the bridge response such as the track irregularities and the contribution of the vehicle–bridge interaction is also taken into account. The results highlight the potential of this approach to obtain satisfactory predictions of the bridge performance in an efficient manner.

1. Introduction

As the demand for more sustainable transportation solutions keeps growing, the capabilities of railway lines are being enhanced due to their green potential. This has led to a sustained interest in predicting the dynamic behaviour of railway bridges to ensure structural safety, optimise bridge design, and manage the structure operation throughout its service life. In this regard, soil–structure interaction (SSI) is a fundamental aspect that can have a notable influence on the dynamic response of railway bridges. This is especially the case for portal frames, as they are partially embedded in the ground, which results in a large portion of the structure being in direct contact with the soil [1]. In this kind of system, the backfill and the surrounding soil provide a notable capacity to dissipate energy through material and radiation damping. Consequently, SSI alters the bridge modal parameters, leading to higher damping ratios [1–5] which usually mitigate vibration levels under moving train loading, especially at resonance [2,6,7]. Therefore, neglecting SSI may be the source of divergences between numerical and experimentally identified bridge responses [2,8]. This could yield unrealistic results when assessing the bridge performance under train passages, inaccurate estimations of the train resonant speed [5,9], misinterpretations of the serviceability limit state of vertical acceleration and, in the end, uneconomical and inefficient structural designs [3].

* Corresponding author.
Email address: chordaj@uji.es (J. Chordà-Monsonís).

https://doi.org/10.1016/j.istruc.2025.110600
Received 22 January 2025; Received in revised form 15 September 2025; Accepted 1 November 2025
Available online 12 November 2025

Despite these implications, SSI is usually disregarded due to the complexity that its simulation entails [2,4] and the absence of realistic information regarding the soil properties. In the works where it is included, two ways of tackling the problem are generally distinguished. First, it can be addressed by solving the entire bridge–soil coupled system, which is known as the direct method. However, addressing the problem in a pure FE approach requires modelling a large portion of the soil domain, which could be impractical due to the high associated computational cost. To improve the efficiency of the calculations, techniques that combine finite elements (FE) and boundary elements (BE) to model the bridge–soil system are frequently employed [6,10,11]. Other options to introduce the dissipative capacity of the soil are based on implementing absorbing boundary conditions, such as, for example, infinite elements (IE) [3,12] or Perfectly Matched Layers (PML) [1,4]. Secondly, SSI can also be conducted in a more practical way for design purposes or parametric studies through a substructuring approach, which consists of analysing the bridge–soil components as separate entities. This permits the isolation and decoupling of the inertial effects of the soil, which can be modelled as series of discrete spring-damper elements representing SSI in simplified models [2,13]. Generally, these spring-dampers are calibrated from mathematical expressions that take into account the geotechnical properties of the soil–foundation system or from dynamic stiffness (or impedance) functions obtained by numerical or experimental techniques.

In the particular case of integral portal frame railway bridges, it is well known that considering SSI is essential to reproduce their dynamic response with accuracy. In recent years, several investigations have been dedicated to this issue. Among them, Galvín and Domínguez [14] implemented a three-dimensional (3D) FE–BE model to analyse the soil motion and the structural response of a portal frame due to passing trains. A decaying law was included to simulate soil damping. The results were accurate and highlighted the importance of simulating the ballast layer in the numerical model. Báez et al. [7] proposed a simplified method to assess the dynamic response of portal frames based on a substructured approach. The FE model was calibrated with experimental data and predictions were precise. Similarly, Vega et al. [15] replicated the response of a portal frame under operating conditions considering two FE coupled models: one for the track superstructure and one for the structure–embankment–soil system. The results were close to the experimental response in the top slab of the bridge. Ülker-Kaustell et al. [16] simulated SSI on a portal frame based on dynamic stiffness functions. The results showed the importance of the soil damping contribution. The authors also concluded that fixing the bridge foundations may lead to underestimating the vertical acceleration at the bridge deck. Zangeneh et al. [2] used a 3D FE model to evaluate the dynamic response of a portal frame. They also proposed a simplified version in which the backfill was simulated by means of linear spring-damper elements. The analyses revealed that the presence of the surrounding soil increased the bridge natural frequency and damping ratio of the vertical bending modes, reducing the resonant response of the bridge. The authors concluded that SSI had a great impact on the structure under study. Salcher et al. [3] used two-dimensional (2D) models to study the influence of SSI on the modal parameters of portal frames. The tests conducted showed a stiffening effect provoked by the soil, which led to an increase in the natural frequency in the first mode involving lateral motion of the frame. A damping increment, mainly affecting the vertical vibrations, was also detected. Zangeneh et al. [1] presented an approach for properly identifying the modal properties of portal frames and filtering out spurious modes of the soil. The procedure was first implemented on a simplified basis and then the results were compared to those provided by a full 3D FE–PML model. Heiland et al. [8] conducted parametric research on portal frame bridges considering: (i) a 2D FE model padded with low-reflection boundaries; (ii) a 3D FE–BE model; and (iii) a 3D substructured model founded on stiffness functions. The results showed the importance of the ratio between the first bending frequency of the frame and the vertical rigid body mode of the soil–foundation system to explain the coupled dynamic soil–bridge behaviour. Heiland et al. [17] studied the dynamic interaction between abutments and their influence on the SSI of a portal frame. The authors proposed a conservative estimation of the frequency range affected by this phenomenon. A 3D FE model which simulated the soil with spring-damper elements was used. The results were validated through experimental testing. Sandqvist and Milicevic [18] investigated the influence of SSI on two medium range portal frames using two 3D FE models with PML layers as absorbing boundaries. The bridge response under dynamic excitation was calculated and compared in different situations considering and neglecting SSI. A simplified version of the models was also implemented. The results revealed that SSI had a key contribution to the global damping of the system and this circumstance could be accentuated in the case of softer soils. Ikzer [19] analysed a short-span portal frame with 3D FE models considering different boundary conditions. The results showed that the simplified approach consisting of dynamic stiffness functions was in good agreement with the outcomes of more complex approaches. Finally, Dagdelen and Ruhani [20] evaluated the SSI on portal frames of different span lengths considering several soil boundary conditions using 2D and 3D FE models. The authors concluded that simulating the backfill was more important in short-span bridges, while for longer structures, the inclusion of the subsoil had a greater impact.

This work is focused on the simulation and analysis of SSI effects in railway bridges. To this aim, a numerical approach is proposed to implement this interaction mechanism with reduced computational effort. The method is based on the research by Galvín et al. [4], devoted to solve the train-induced vibration problem in simple beam-type bridge models while considering SSI. In this study, this approach is expanded and adapted to be applied to more complex bridge configurations. The procedure in question is substructured. This implies that the bridge–soil system is analysed in a decoupled manner in relation to SSI. Based on this premise, two 3D FE numerical models are implemented. The first one represents a comprehensive idealisation of the full track–bridge–soil integrated system, and is used to replicate SSI in a detailed manner. This allows the derivation of dynamic stiffness (or impedance) functions at the bridge–soil interface. These frequency-dependent functions represent the inertial behaviour of the soil, capturing its resistance to the bridge motion and the energy exchange with the structure in the contact area between both elements. Subsequently, a simplified version of the previous model is implemented. In this variant, the soil domain is not explicitly simulated, but is rather introduced as a series of linear spring-damper elements that are calibrated from the stiffness and damping properties of the previously calculated dynamic stiffness functions. With this approach, SSI is incorporated into the simplified model without the necessity of simulating the soil domain, which, due to its large size in terms of degrees of freedom (DOFs), is the main factor contributing to the increase in computational cost. Then, the bridge dynamic response under operating conditions can be computed by means of complex modal superposition (CMS), leading to relatively fast calculations.

In this manner, the main objective of this contribution is to present, implement, and validate this approach to simulate SSI in an efficient way. The methodology in question is applied to the case of an existing portal frame railway bridge in order to study its dynamic response while considering SSI. In this sense, it is also intended to (i) identify its modal parameters from experimental data, (ii) evaluate its performance under operating conditions, and (iii) discuss the influence of other factors such as the track irregularities and the artificial increment of the bridge damping to include the effect of the vehicle–bridge interaction (VBI), as a set of complementary objectives of the work. These aspects are also relevant, as, although portal frames are a well-established constructive solution, no special attention has been paid to their dynamic study until recent times [15]. Consequently, there are issues yet to be addressed in relation to the most appropriate analysis techniques to be used in this regard. As previous research has pointed out, there is a lack

Fig. 1. Images of the underpass under study: (a–b) the bridge, seen from the HS side, (c) a satellite image of the structure [22], and (d) a view of the bridge deck next to the conventional track.

of straightforward modelling procedures to simulate SSI and avoid excessive time-consuming analyses [21]. Besides, literature incorporating validation of numerical results against in-field data is rather limited [2], especially when focused on evaluating the bridge dynamic behaviour.

For these reasons, the current investigation addresses important aspects in relation to SSI implementation and the bridge typology under examination. Ultimately, a simplified method to simulate SSI could bring further insight into the influence of this interaction mechanism on the dynamic response of railway bridges. Besides, in relation to portal frames, a full understanding of the effect of SSI could be useful, as these bridges are the predominant type of underpass in modern railway lines [2,3,7] and their usage is widespread. Therefore, predicting their dynamic response with accuracy could be beneficial to assess the performance of existing structures when facing new traffic requirements and to avoid overly conservative predictions of the bridge response in the design phase of new bridges that could lead to suboptimal and costly solutions.

This paper is organised as follows. In Section 2, the bridge under study is presented, and the identification of the modal parameters is explained. In Section 3, the proposed numerical approach is described, together with the main characteristics of the numerical models. Next, the mathematical formulation of the SSI problem, including the track irregularities and the bridge damping incorporated to implement VBI, is detailed in Section 4. Subsequently, the results obtained are presented and validated in Section 5. Lastly, the conclusions of this work are summarised in Section 6.

2. Bridge under study

2.1. Structure description

The Camino de las Huertas underpass is a portal frame railway bridge. It is situated on the Madrid–Sevilla high-speed (HS) line within the Ciudad Real–Brazatortas section at kilometric point 31 + 200. The structure spans 8 m in length and 22.1 m in width. Its cross section consists of a reinforced concrete rectangular integral box. The bridge is traversed by three tracks composed of UIC60 rails. Two of them provide HS services and feature standard gauge with monoblock sleepers. The remaining track is used to connect the cities of Ciudad Real and Badajoz with trains circulating at conventional speed. This track features Iberian gauge with twin-block sleepers. The constructive characteristics of this portal frame are peculiar, as it is divided along its width by a narrow longitudinal joint located between the HS and the conventional tracks. This results in two separate but weakly connected structures that, nevertheless, remain dynamically coupled in certain frequency ranges, as it will be shown later on. Several views of the bridge are shown in Fig. 1(a–d).

2.2. Experimental programme

In-situ experimental measurements were conducted in September 2022 to identify the modal parameters and the dynamic response of the bridge under operating conditions. The accelerometers were installed on the inner walls of the portal frame. First, the concrete surface was cleaned and sanded. Then, an accelerometer aluminium base featuring an internal thread was bonded to the bridge slab using adhesive. Finally, once the base was securely attached, the sensor was screwed into place, completing the installation. The attached accelerometers can be seen in Fig. 2, where two images of the setup during the experimental campaign are shown. In Fig. 2(a), the longitudinal joint can be distinguished as a dark line on the bridge slab in the location indicated by the arrows. In Fig. 2(b), part of the adhesive used to glue the accelerometer base can be distinguished around this element.

In total, 27 piezoelectric accelerometers with a nominal sensitivity of 10 V/g were arranged as indicated in Fig. 3: 18 were attached to the top slab (shown in red), 6 on the walls (shown in yellow) and 3 on the bottom slab (shown in blue). Sensors on both slabs registered data in the vertical direction, whilst those on the walls measured horizontal motion. Based on this scheme, the dynamic response of the structure was recorded under the passage of 27 trains and under ambient vibration. The bridge dimensions are also depicted in Fig. 3, where the vertical dashed line represents the location of the longitudinal joint.

2.3. Modal identification

The modal parameters of the bridge were identified by means of an Operational Modal Analysis (OMA). To this aim, the measurements from

Fig. 2. Bridge setup during the experimental campaign: (a) sensors on the slab, where the white arrows mark the position of the longitudinal joint, and (b) an accelerometer installed at the bridge wall. (For interpretation of the references to colour in this figure legend, the reader is referred to the web version of this article.)

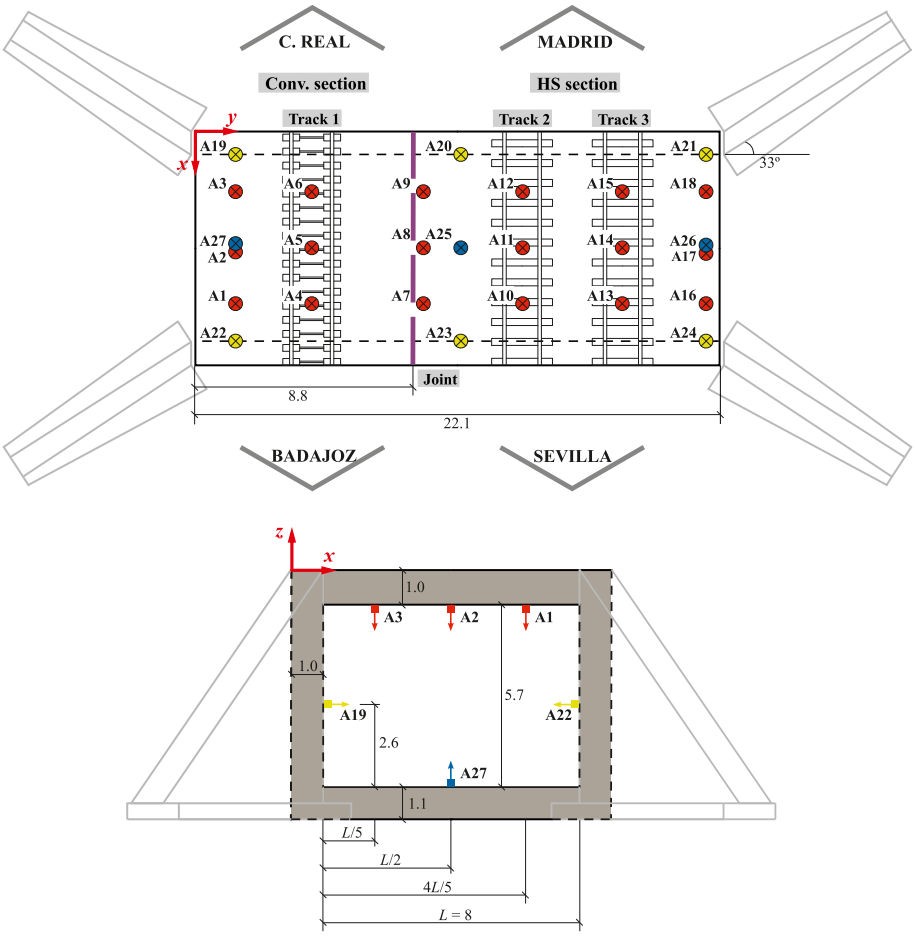

Fig. 3. Accelerometer layout and dimensions of the portal frame.

the structural response under ambient conditions combined with part of the free vibrations of the bridge after passing trains were used as input data. This facilitated the identification process and reduced the complexity of the problem, as an initial test using just the data from ambient vibration led to inconclusive results due to the low amplitudes associated. The experimental recordings of the bridge under ambient vibration had a duration of 3300 s, and were acquired at a sampling frequency of 4096 Hz. The signal was decimated to 256 Hz and a high-pass Chebyshev filter of 1 Hz was applied. On the other hand, segments of the bridge free vibration after the train crossings were extracted from the complete passage recordings and concatenated into a continuous signal with a total duration of approximately 100 s, which was filtered with a high-pass Chebyshev filter of 10 Hz. These measurements were also acquired at a sampling frequency of 4096 Hz and decimated to 256 Hz. As an example, the ambient vibration registered in accelerometer A5 is shown in Fig. 4(a and b), whereas the bridge free response after a train passage is shown in Fig. 4(c and d). In these graphs, the root mean square (RMS) acceleration is computed considering a time window of 1 s, as prescribed by ISO 2631 [23].

In this manner, the OMA was conducted and the bridge modal properties were identified by means of the Enhanced Frequency Domain Decomposition (EFDD) method [24]. The corresponding singular value decomposition (SVD) graph is shown in Fig. 5.

The estimated modal parameters of the bridge are shown in Fig. 6, where the dashed line indicates the joint location. The first and third mode shapes are the fundamental bending modes of the HS and

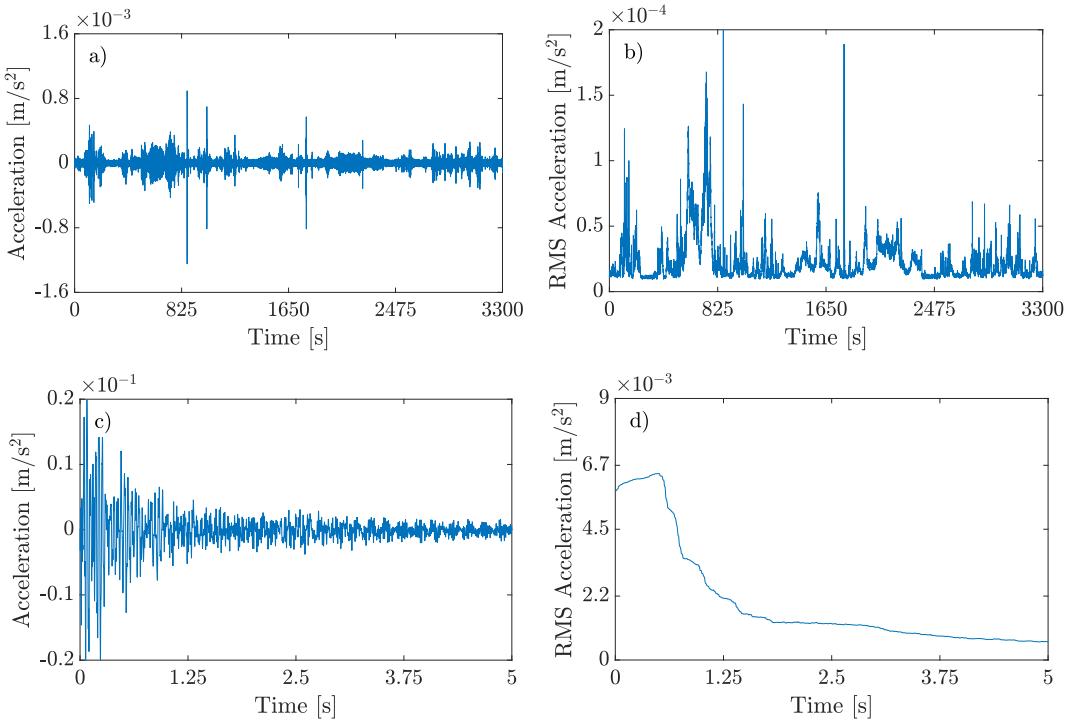

Fig. 4. Example of the time-history and RMS acceleration of the data registered in accelerometer A5: (a) and (b) correspond to the ambient vibration, and (c) and (d) to the free vibrations of the bridge after a train crossing.

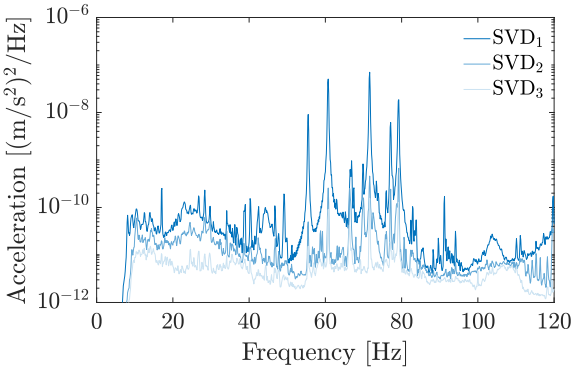

Fig. 5. SVD plot of the OMA conducted on the portal frame under study.

conventional speed sections, respectively. In these modes, the vertical movement of the bridge deck in the longitudinal direction is characteristic and tends to attenuate near the joint. In a similar way, the walls and the bottom slab undergo a certain degree of convex warping that is mostly limited within the corresponding bridge part. The second mode is close in terms of frequency to the third one. However, in f_2, a more pronounced deformation is observed in the HS region, occurring at a significant distance from the longitudinal joint and affecting both the deck and the bridge walls. At higher frequencies, as the width of the portal frame is significantly larger than its length, the structural displacement describes transverse bending modes. Accordingly, modes of this type such as f_4, f_6, f_7 and f_8 are more associated with the conventional zone, whereas f_9, f_{10} and f_{11} have a predominant movement in the HS area. Other cases such as f_2 and f_5 are examples of moderately coupled modes in which the participation of both bridge sections is apparent. These results describe the asymmetric dynamic nature of the structure, in which decoupled modes coexist with others in which both sections contribute to the overall structural behaviour. It should also be noted that owing to the bridge extension, a certain degree of spatial aliasing may be present on the estimated mode shapes due to the number of accelerometers employed. This situation may be more accentuated in the walls and the bottom slab and at higher frequencies. Better results are obtained in the top slab, where more precision is achieved.

To obtain a realistic approximation of the modal damping, the recordings of the bridge free vibration response after passing trains were evaluated. This procedure was followed because the damping assessment is highly dependent on the amplitude of the measured vibrations [25]. Therefore, a more representative estimation was expected after dynamic train loading, as this excitation could activate more energy-dissipating mechanisms within the bridge–soil system. In this way, based on the method described in Reference [26], the Random Decrement Technique (RDT) [27] was first applied to process the measured acceleration signal and obtain the corresponding impulse response function (IRF), which describes the structure performance over time. Subsequently, damping was calculated by fitting an exponential decay to the IRF envelope. This approach was employed to conduct a comprehensive analysis on data from all sensors available considering the totality of the registered train passages. Final damping values, shown in Fig. 6 for each mode, were obtained after averaging the results and filtering out possible outliers to ensure the adequacy of the solution. The results obtained reveal higher damping ratios in comparison to those provided in Eurocode (EC) [28] for prestressed concrete bridges, particularly for the lower modes.

3. Numerical approach

The procedure presented to simulate SSI with an admissible computational cost is based on a substructuring approach. For this purpose, two numerical models are used to represent the portal frame under study. To begin with, a full track–bridge–soil interaction model is implemented to derive dynamic stiffness functions at the bridge–soil interface. This data

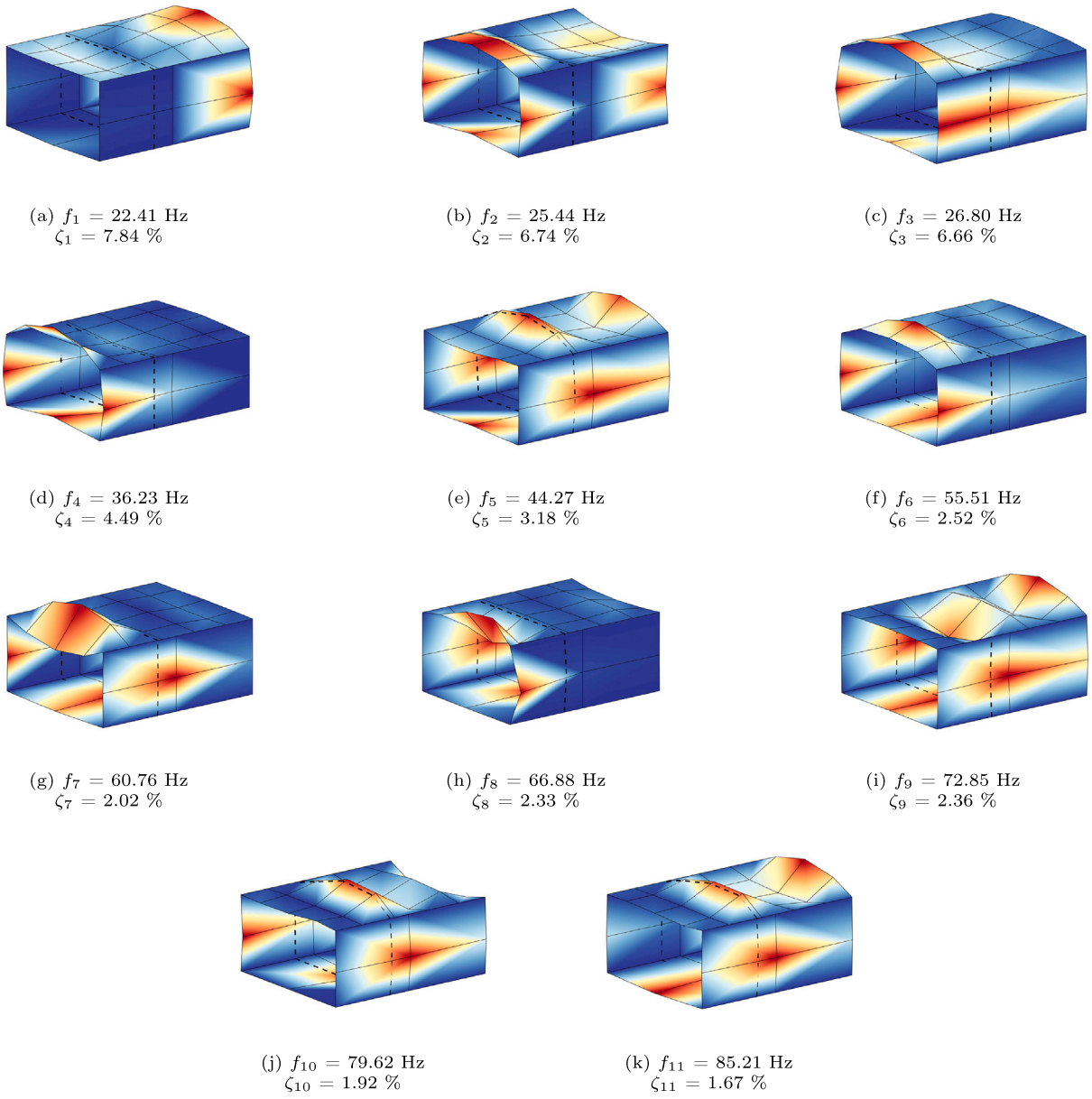

(a) $f_1 = 22.41$ Hz, $\zeta_1 = 7.84$ %
(b) $f_2 = 25.44$ Hz, $\zeta_2 = 6.74$ %
(c) $f_3 = 26.80$ Hz, $\zeta_3 = 6.66$ %
(d) $f_4 = 36.23$ Hz, $\zeta_4 = 4.49$ %
(e) $f_5 = 44.27$ Hz, $\zeta_5 = 3.18$ %
(f) $f_6 = 55.51$ Hz, $\zeta_6 = 2.52$ %
(g) $f_7 = 60.76$ Hz, $\zeta_7 = 2.02$ %
(h) $f_8 = 66.88$ Hz, $\zeta_8 = 2.33$ %
(i) $f_9 = 72.85$ Hz, $\zeta_9 = 2.36$ %
(j) $f_{10} = 79.62$ Hz, $\zeta_{10} = 1.92$ %
(k) $f_{11} = 85.21$ Hz, $\zeta_{11} = 1.67$ %

Fig. 6. Estimated modal parameters of the portal frame.

feeds a simplified model, which is later integrated by complex modal time-history analysis.

3.1. Track–bridge–soil full interaction model

First, a detailed 3D FE numerical model of the portal frame is implemented in ANSYS (R) v.22.1 to provide an accurate representation of the SSI problem. The model, shown in Fig. 7(a), comprises the track, the bridge and the surrounding soil. Starting from the track, the rails are meshed as Timoshenko beam elements with 6 DOFs per node (BEAM188). The relative vertical displacement between the rails and the sleepers is linked through the rail pads, which are included as spring-damper elements (COMBIN14) with constant vertical stiffness and viscous damping. The resultant vertical force is transmitted by means of kinematic constraints distributed over the contact area between the rail pads and the sleepers, which are modelled with half of their height embedded in the ballast layer. Both ballast and sleeper materials are considered elastic and isotropic and are meshed with solid finite 3D elements (SOLID185). In the case of the twin-block sleepers, the steel crossbar in between the blocks is meshed using BEAM188 elements. The presence of other non-structural features such as handrails are also included in the model as lumped masses (MASS21) uniformly distributed along each side of the deck.

Below the track, the portal frame structure and the longitudinal joint are represented with shell elements (SHELL181). On the other hand, the soil domain (including the backfill) is meshed with SOLID185 elements. To avoid spurious wave reflections and simulate the dissipative effect of the terrain, the model boundaries are padded with three layers of solid PML elements. This procedure allows for reducing the amount of soil required to simulate SSI in a correct manner and the computational cost needed for the calculations. Adequate soil and PML lengths are derived from convergence studies as $L_{\text{soil}} = 7.5$m and $L_{\text{PML}} = 0.5$m (see Fig. 7(b)), respectively, to ensure the adequacy of the results. The mesh in the PML region is discretised to fit a sufficient number of elements per wavelength ($\lambda = 2\pi C_s/\omega$), where C_s is the propagation velocity of the shear waves within the soil and ω is the highest identified frequency of the bridge [29]. In total, the model has 1,340,132 DOFs.

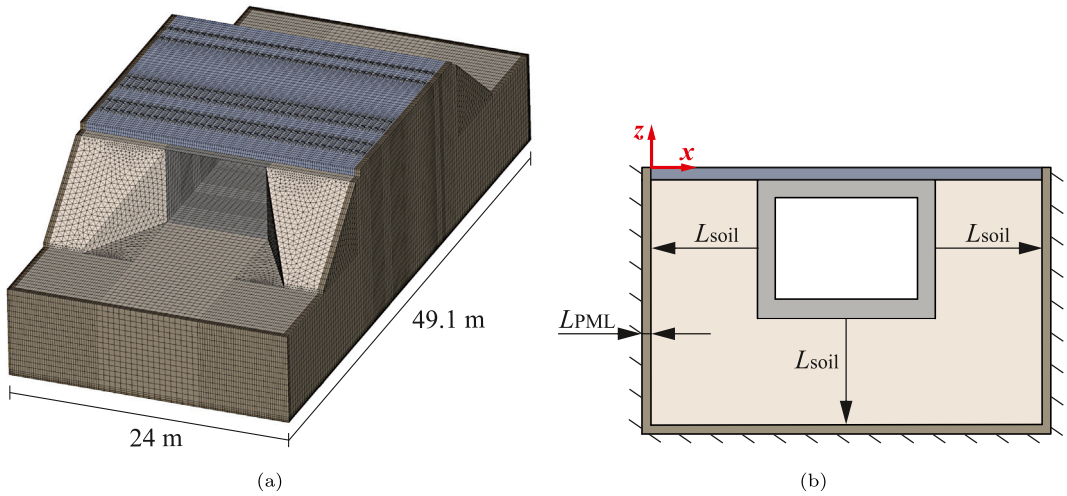

Fig. 7. Details of the full track–bridge–soil interaction model: (a) image of the FE discretisation, and (b) soil and PML lengths.

The mechanical properties of the model are listed in Table 1. Among the track components, the following parameters are provided. In the rails, E_r is the elastic modulus, I_{ry} corresponds to the moment of inertia with respect to the y axis and m_r is the linear mass. The stiffness and damping associated with the rail pads are denoted as K_p and C_p, respectively. Monoblock and twin-block sleepers differ in terms of geometry. Dimensions regarding their length, width and height are listed. The distance between consecutive sleepers is represented as D_{sm} and D_{st} for each sleeper type and is equal to 0.6 m in both cases. The height of the ballast layer is denoted as h_b and is assumed constant and uniform over the bridge deck. A value of $h_b = 72.8$ cm is considered based on visual inspection and in-situ measurements. Beneath the sleepers, the ballast thickness equals $h_b - h_{si}/2$, with h_{si} being the height of the corresponding sleeper type. In any case, the result is in accordance with the minimum ballast thickness required by the IF3 Spanish standard [30].

With regard to the portal frame properties, the elastic modulus of the slab is obtained from the construction project of the structure [31]. Despite the importance of the longitudinal joint in the bridge modal behaviour (see Fig. 6), the calibration of this parameter presented a high level of uncertainty, as the information available about it was very limited. For this reason, several modal analyses were carried out to adjust the elastic modulus of the joint material E_j. The final value listed in Table 1 provides an adequate degree of coupling between the two bridge sections and allows to reproduce the identified modal parameters of the portal frame.

Lastly, the entire soil domain is conceived as a homogeneous elastic half-space. The authors had access to geotechnical reports where estimations of the soil density were provided [32]. Other documents contained results from various Standard Penetration Tests (SPTs) conducted around the bridge site before its construction, potentially indicating the presence of a moderate to high stiff soil. However, the information was insufficient to characterise key soil parameters such as C_s with enough precision. In light of this, this parameter was calibrated from a series of preliminary modal analyses. To this aim, despite the soil properties not being measured during the experimental campaign, the authors had previously studied the soil strata of Jabalón bridge, a structure located 20 km away from the portal frame, as reported in [25]. Based on this and other references [1,15,33], a range of possible C_s values was determined. Then, the full track–bridge–soil interaction model was used to perform several modal analyses applying variations to C_s with the objective of assessing whether the experimental bridge modes were predicted at the right frequencies. Satisfactory results in this regard were obtained considering a shear wave propagation speed of $C_s = 350$ m/s. The updated value of C_s falls within the scope of possibilities derived from the geotechnical reports and with the observations in Jabalón bridge [25].

3.2. Simplified track–bridge–soil interaction model

Next, a simplified version of the previous model is implemented. This step involves the inertial decoupling of the surrounding soil from the track–structure system and enables simulating SSI with optimal computation time. For this reason, only the track and the bridge are considered and meshed as indicated in the previous section and shown in Fig. 8(a). Conversely, the soil domain is substituted by a series of discrete linear frequency-dependent spring-dampers. These elements are arranged over 65 points uniformly distributed over the soil–bridge interface at the vertical walls and bottom slab of the portal frame. At each point, three spring-dampers are attached: one perpendicular and two tangential to the surface, following the three spatial directions (x, y, z) as shown in Fig. 8(b). With regard to the boundary conditions, the nodes of the bottom ballast area under the track extensions are considered clamped to isolate SSI effects on the bridge. As a result of this decoupling procedure, a reduced-order 3D FE model with 175,904 DOFs is obtained, a substantial reduction in comparison to the full model.

3.3. Modal updating

The spring-dampers utilised in the simplified model are calibrated by means of dynamic stiffness functions. The procedure described below to calculate them is similar to those presented in References [18,19], where this type of function is used to model the vertical interaction of the bridge slab with the soil beneath it. However, in the cited studies, a different approach is followed to model the wall–backfill interaction (wherein additional non-linearities may emerge) based on correlations that incorporate the geotechnical properties of the terrain [2]. In the present work, the method proposed is employed for all the spring-damper elements, independently of their location.

In this way, as schematised in Fig. 9, the soil–bridge dynamic behaviour is characterised by means of a harmonic analysis conducted in the full interaction model. A vertical distributed force $F_s(\omega)$ is applied on both rails of track 2 covering the bridge span length. In the same figure, the calculation points, represented as white squares, are the positions where the spring-dampers will be attached in the upcoming simplified model. For this reason, in each calculation point, three dynamic stiffness functions are computed to define the properties of the three associated spring-damper elements (one in each direction x, y and z). These functions are computed as the quotient between the resultant of the vertical force and the measured displacement in the corresponding

Table 1
Mechanical properties of the full track–bridge–soil interaction model. Note that (M-b) and (T-b) stand for monoblock and twin-block.

Entity	Part	Property	Notation	Value	Unit	Reference
Track	Rail UIC 60	Elastic modulus	E_r	2.10×10^{11}	Pa	[34]
		Moment of inertia	I_{ry}	3038×10^{-8}	m^4	[34]
		Linear mass	m_r	60.34	kg/m	[34]
	Rail pad	Stiffness	K_p	1.00×10^8	N/m	[35]
		Damping	C_p	7.50×10^4	Ns/m	[35]
	Sleepers (M-b)	Elastic modulus	E_{sm}	3.60×10^{10}	Pa	[36]
		Poisson's ratio	ν_{sm}	0.2	–	
		Mass	m_{sm}	320	kg	[36]
		Length	l_{sm}	2.6	m	[36]
		Width	w_{sm}	0.3	m	[36]
		Height	h_{sm}	0.24	m	[36]
		Distance	D_{sm}	0.6	m	[36]
	Sleepers (T-b)	Elastic modulus	E_{st}	3.60×10^{10}	Pa	[36]
		Poisson's ratio	ν_{st}	0.2	–	
		Mass	m_{st}	200	kg	[36]
		Length	l_{st}	2.5	m	[36]
		Width	w_{st}	0.29	m	[36]
		Height	h_{st}	0.2	m	[36]
		Distance	D_{st}	0.6	m	[36]
		Cross bar elastic modulus	E_{str}	2.10×10^{11}	Pa	[37]
	Ballast	Elastic modulus	E_b	1.10×10^8	Pa	[38]
		Poisson's ratio	ν_b	0.2	–	[39]
		Density	ρ_b	1950	kg/m^3	[38]
		Height	h_b	0.728	m	[30]
Bridge	Slab	Elastic modulus	E_u	3.57×10^{10}	Pa	[31]
		Poisson's ratio	ν_u	0.2	–	
		Density	ρ_u	2500	kg/m^3	[40,41]
	Longitudinal joint	Elastic modulus	E_j	9522.50	Pa	
		Poisson's ratio	ν_j	0.2	–	
		Density	ρ_j	2500	kg/m^3	
	Handrail	Linear mass	m_h	50	kg/m	[40]
Soil	Soil and backfill	Elastic modulus	E_s	5.73×10^8	Pa	
		Poisson's ratio	ν_s	0.2	–	
		Density	ρ_s	1950	kg/m^3	[32]
		Shear wave speed	C_s	350	m/s	

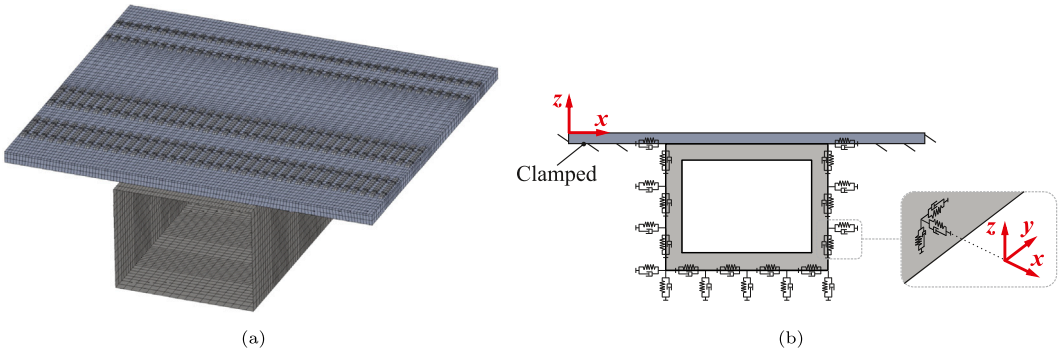

Fig. 8. The simplified track–bridge–soil interaction model: (a) image of the model discretised in FE, and (b) schematic front view including the spring-dampers.

direction i: $Z^s_{d,i}(\omega) = F_s(\omega)/U_i(\omega)$. Given that the load and the displacement are out of phase due to the inertial and damping properties of the soil, the results of this operation are complex. Subsequently, it is possible to obtain the properties of stiffness $K_i(\omega) = \mathrm{Re}[Z^s_{d,i}(\omega)]$ and viscous damping $C_i(\omega) = \mathrm{Im}[Z^s_{d,i}(\omega)]/\omega$ to be implemented as spring-damper elements in the simplified model [4].

The results obtained from this analysis are dependent on the frequency. In this sense, Fig. 10(a–c) show the displacement at points P1 and P2 in x, y and z in absolute value for the frequency range between 1 and 100 Hz. These calculation points are located halfway up the bridge wall, as shown in Fig. 9. The points are found on opposite sides of the longitudinal joint, therefore belonging to different bridge sections. The separation between them is of 5.5 m, approximately. Fig. 10(a–c) show that maximum displacement peaks occur near the fundamental frequency of the bridge ($f_1 = 22.41$ Hz, as indicated by the dashed line) in the vertical (z) but also in the longitudinal (x) direction. This is in accordance with the behaviour observed in the first experimental mode, as it involves the convex warping of the vertical bridge walls. The response in the transverse direction (y) is less significant in this case. Other prominent peaks are related to higher structural modes. The displacement amplitudes in the longitudinal and vertical directions are higher at P2 when compared to P1. This occurs because P2 is situated in the

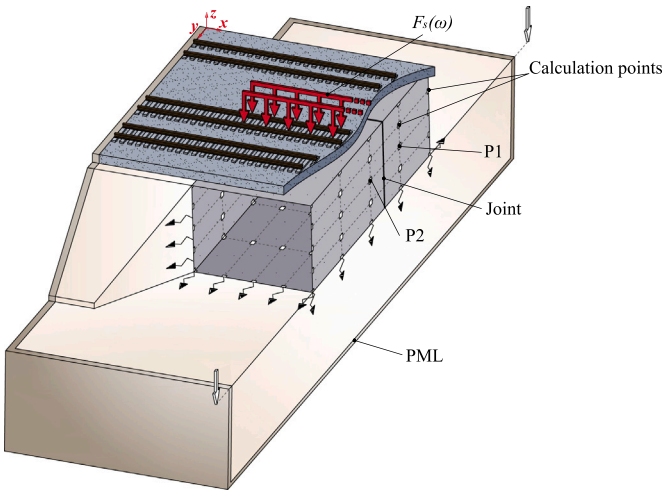

Fig. 9. Scheme of the harmonic analysis conducted to compute the dynamic stiffness functions at the calculation points.

HS section, where the dynamic load is being applied. However, part of this result is also attributable to the decoupling effect of the joint, that hinders the energy transmission throughout the bridge slab.

Derived from the calculated harmonic displacement, the corresponding stiffness and damping curves are shown in Fig. 10(d–f) and (g–i), respectively. In both calculation points, prominent peaks occur in high frequency ranges. Nevertheless, P1 presents a more oscillating trend

Table 2
Mechanical properties of the bridge sections before and after calibration.

Parameter	Bridge section	Nominal	Updated	Variation	Unit
Ballast density	Conventional	1950	1560	−20 %	kg/m^3
	High-speed		2340	+20 %	
Slab elastic modulus	Conventional	35.71	30.35	−15 %	GPa
	High-speed		26.07	−27 %	

with multiple spikes in $|K_x|$ and $|K_z|$ in the interval between 40 and 100 Hz. In comparison, nearing the fundamental mode of the bridge, differences between P1 and P2 are less important and the values attain certain stability. In view of this, the properties of stiffness and damping are finally tuned to the fundamental frequency of the bridge to reduce the variability among the parameters under calculation.

An additional calibration step is carried out to complete the process. The authors found that in order to replicate the asymmetric modal behaviour detected in Section 2.3, it was necessary to differentiate the mechanical properties of both bridge sections. In this way, the adjustment is performed on the ballast density and on the elastic modulus of the slab. The updated parameters are listed in Table 2. After this calibration, the properties of the spring-dampers are accordingly recalculated. The variation with respect to the previous values was acceptable. Besides, it was also observed that the final results involving the bridge response due to train passages were not sensitive to small variations of the spring-damper properties such as the ones considered in this step, leading to stable results.

With this configuration, a complex modal analysis is conducted employing the simplified model. The resultant modal parameters are

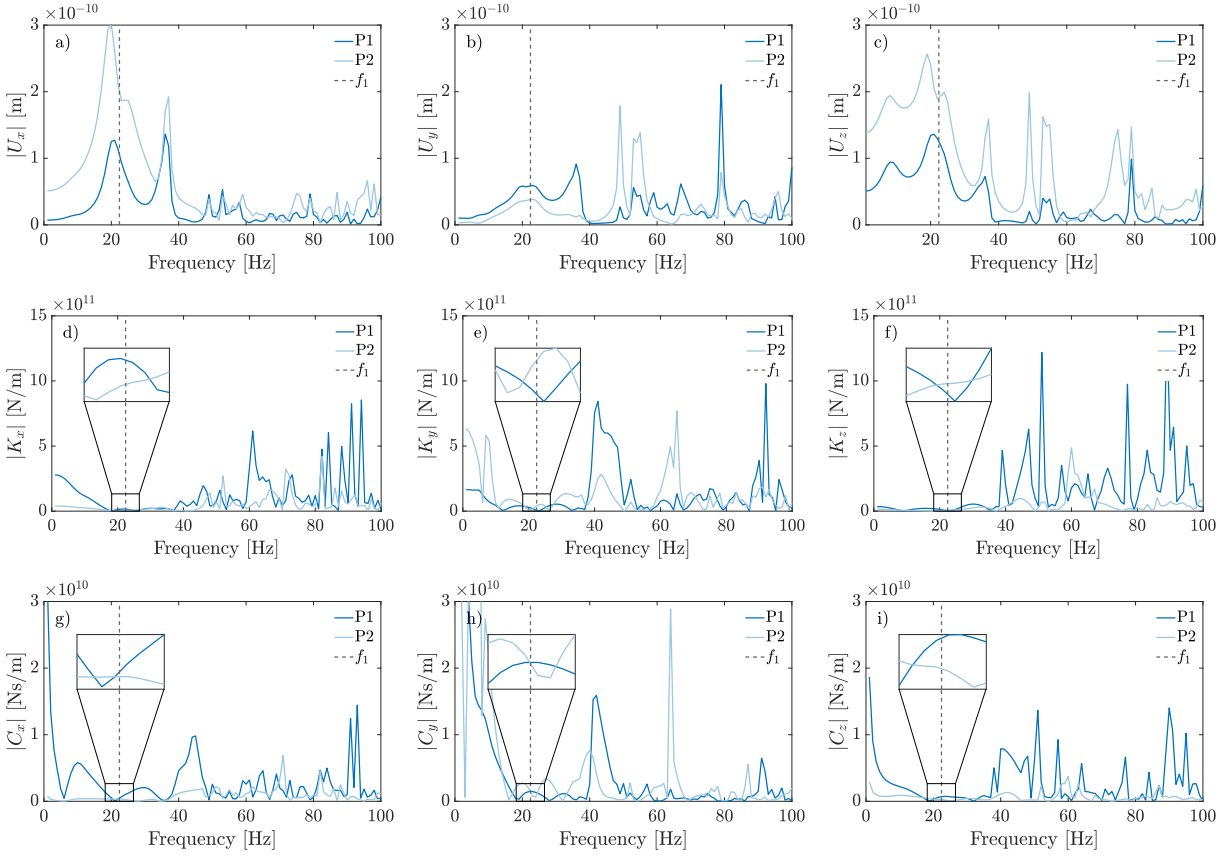

Fig. 10. Results of the harmonic analysis conducted to characterise SSI in the full track–bridge–soil interaction model at P1 and P2: (a–c) displacement in each direction, (d–f) stiffness, and (g–i) viscous damping.

Table 3
Experimental–numerical comparison of the bridge modal parameters. Modes 9 and 10 do not have any numerical counterpart.

Mode	f_i^{exp} [Hz]	f_i^{num} [Hz]	e_i [%]	MAC
f_1	22.41	22.23	−0.8	0.611
f_2	25.44	25.59	0.6	0.483
f_3	26.80	26.93	0.5	0.740
f_4	36.22	34.05	−6.0	0.694
f_5	44.27	37.38	−15.6	0.769
f_6	55.51	63.57	14.5	0.811
f_7	60.76	60.94	0.3	0.878
f_8	66.88	65.25	−2.4	0.881
f_9	72.85	–	–	–
f_{10}	79.62	–	–	–
f_{11}	85.21	72.50	−14.9	0.832

compared to their experimental counterparts in Table 3, where the first column indicates the mode under comparison. The second and third columns list the empirical and the numerical damped frequencies, respectively, and the fourth one indicates the difference between these two values in percentage. In the fifth column, the modal assurance criterion (MAC) is calculated considering the accelerometers underneath the top slab (A1–A18) and is used to assess the similarity between pairs. Then, Fig. 11 provides a comparison of the mode shapes. Experimental ones are depicted in black, whereas numerical ones are shown in gray. The representation corresponds to the real part of the complex eigenvector.

Resulting from this procedure, all the experimental modes have been satisfactorily predicted employing the numerical model, except for modes 9 and 10 (see Fig. 6). As can be seen, a reasonably good agreement is achieved in terms of frequencies in the majority of the modes. The highest divergence in absolute value is observed in f_5 with a value of 15.6 %. Nonetheless, a difference lower than 3 % is achieved in 5 modes: f_1, f_2, f_3, f_7 and f_8, being less than 1 % in the first four cases. The MAC values also indicate a satisfactory degree of correlation, especially among the highest modes.

4. Formulation of the SSI moving load dynamic problem

This section addresses the solution of the SSI problem, which is approached as follows. First, a modal analysis is performed on the simplified interaction model and the mode shapes are retrieved from ANSYS (R) v.22.1. Due to the presence of the spring-dampers, the results obtained are complex. Non-oscillatory modes with real eigenvalues are discarded. Subsequently, complex modes and natural frequencies are exported to MATLAB (R) v.2024 a to solve the SSI problem by means of CMS. Then, the bridge response under passing trains is computed [42]. To proceed in this manner, an intermediate normalisation step is necessary to operate with the mode shapes retrieved from ANSYS.

Thus, in the first part of this section, the formulation of the SSI problem is presented. In the second part, the changes conducted in the normalisation of the mode shapes are explained. On the other hand, the excitation mechanisms used to simulate train induced vibrations are detailed in the third part of the section. Finally, the fourth part delves into the additional amount of structural damping considered to account for VBI.

4.1. Problem formulation

The equilibrium equation of the bridge FE model, comprising N DOFs, with initial conditions of displacement $\mathrm{u}(0) = \mathrm{u}_0$ and velocity $\dot{\mathbf{u}}(0) = \dot{\mathbf{u}}_0$, is:

$$\mathbf{M}\ddot{\mathbf{u}}(t) + \mathbf{C}\dot{\mathbf{u}}(t) + \mathbf{K}\mathbf{u}(t) = \mathrm{F}(t) \tag{1}$$

where M, C and K represent the mass, damping and stiffness matrices of the problem. The effect induced by the spring-dampers at the domain contour makes the global damping of the system non-proportional, which implies that $(\mathrm{M}^{-1}\mathrm{C})(\mathrm{M}^{-1}\mathrm{K}) \neq (\mathrm{M}^{-1}\mathrm{K})(\mathrm{M}^{-1}\mathrm{C})$ and results in complex modes. In this context, the position of each DOF is defined by amplitude and phase angle. Thus, a set of 2 N equations is required to evaluate the solution of the N DOF of the structure. In this sense, Eq. (1) can be rewritten as a system of 2 N equations:

$$\begin{bmatrix} \mathrm{C} & \mathrm{M} \\ \mathrm{M} & \mathbf{0} \end{bmatrix} \begin{bmatrix} \dot{\mathbf{u}}(t) \\ \ddot{\mathbf{u}}(t) \end{bmatrix} + \begin{bmatrix} \mathrm{K} & \mathbf{0} \\ \mathbf{0} & -\mathbf{M} \end{bmatrix} \begin{bmatrix} \mathbf{u}(t) \\ \dot{\mathbf{u}}(t) \end{bmatrix} = \begin{bmatrix} \mathrm{F}(t) \\ \mathbf{0} \end{bmatrix} \tag{2}$$

which can be expressed as a first order differential matrix equation:

$$\mathbf{A}\dot{\mathbf{y}}(t) + \mathbf{B}\mathbf{y}(t) = \mathbf{P}(t) \tag{3}$$

where A and B are two real and symmetric matrices of dimensions $2N \times 2N$ and y is the state vector:

$$\mathrm{A} = \begin{bmatrix} \mathrm{C} & \mathrm{M} \\ \mathrm{M} & \mathbf{0} \end{bmatrix} \quad \mathrm{B} = \begin{bmatrix} \mathrm{K} & \mathbf{0} \\ \mathbf{0} & -\mathbf{M} \end{bmatrix} \quad \mathrm{P} = \begin{bmatrix} \mathrm{F}(t) \\ \mathbf{0} \end{bmatrix} \quad \mathrm{y}(t) = \begin{bmatrix} \mathrm{u}(t) \\ \dot{\mathbf{u}}(t) \end{bmatrix} \tag{4}$$

In the free vibration case, Eq. (3) yields:

$$\mathbf{A}\dot{\mathbf{y}}(t) + \mathbf{B}\mathbf{y}(t) = \mathbf{0} \tag{5}$$

In this system of linear equations, the non trivial solution can be obtained as $\mathrm{y}(t) = \boldsymbol{\Psi}_j e^{s_j t}$, where s_j is the j-th of $2N$ eigenvalues and $\boldsymbol{\Psi}_j$ is the corresponding eigenvector:

$$\boldsymbol{\Psi}_j = \begin{bmatrix} \boldsymbol{\phi}_j \\ s_j \boldsymbol{\phi}_j \end{bmatrix} \tag{6}$$

Then, natural frequencies, damped natural frequencies and modal dampings can be calculated from the eigenvalues as $\omega_j = |s_j|$, $\omega_{dj} = |\mathrm{Im}[s_j]|$ and $\zeta_j = -\mathrm{Re}[s_j]/|s_j|$, respectively. Following, in the forced vibration case, the solution to Eq. (3) can be expressed as:

$$\mathrm{y}(t) = \sum_{j=1}^{2N} \boldsymbol{\Psi}_j z_j(t) \tag{7}$$

If orthogonality conditions $\boldsymbol{\Psi}_j^T \mathrm{A} \boldsymbol{\Psi}_k = 0$ and $\boldsymbol{\Psi}_j^T \mathrm{B} \boldsymbol{\Psi}_k = 0$ are satisfied for any pair of modes $j \neq k$ (where superscript T indicates matrix transpose) and the eigenvectors are normalised to the A matrix (i.e., $\boldsymbol{\Psi}_j^T \mathrm{A} \boldsymbol{\Psi}_j = 1$), Eq. (3) results into a set of $2N$ uncoupled equations [42]:

$$\dot{z}_j(t) + \alpha_j z_j(t) = p_j(t) \tag{8}$$

where $p_j(t) = \boldsymbol{\Psi}_j^T \mathrm{P}(t)$ and α_j is later defined in Eq. (14). This is a non-stiff differential equation that can be solved numerically. In the present work, the solution to this equation is computed by means of a Runge–Kutta (4,5) explicit algorithm [43,44]. Then, CMS is used to calculate the bridge displacement as indicated in the equation below. This expression takes into account that the eigenvalues and eigenvectors in the analysis under consideration are pairs of complex conjugates.

$$\mathrm{u}(t) = \sum_{j=1}^{N} 2\mathrm{Re}[\boldsymbol{\phi}_j z_j(t)] \tag{9}$$

4.2. Mode shapes normalisation

To proceed with the calculations as indicated in the previous section, it is necessary to address the normalisation of the mode shapes computed with ANSYS. In this case, the modes are obtained via complex modal analysis and normalised by default to the mass matrix M. As the mode shapes are exported to MATLAB to solve the moving load problem, they need to be normalised to the A matrix. To this aim, a scaling parameter allowing this operation to be performed is derived. Initially, the mode shapes are normalised to the mass matrix. In the subsequent formulation, this is indicated by the M superscript. Thus, they fulfil that $\boldsymbol{\Psi}_j^{T,M} \mathrm{A} \boldsymbol{\Psi}_j^M \neq 1$. Taking into account Eqs. (4) and (6), and if the previous condition is further developed, this can be expressed as:

$$\boldsymbol{\Psi}_j^{T,M} \mathrm{A} \boldsymbol{\Psi}_j^M = \begin{bmatrix} \boldsymbol{\phi}_j \\ s_j \boldsymbol{\phi}_j \end{bmatrix}^{T,M} \begin{bmatrix} \mathrm{C} & \mathrm{M} \\ \mathrm{M} & \mathbf{0} \end{bmatrix} \begin{bmatrix} \boldsymbol{\phi}_j \\ s_j \boldsymbol{\phi}_j \end{bmatrix}^{M} = \boldsymbol{\phi}_j^{T,M} \mathrm{C} \boldsymbol{\phi}_j^M + 2 m_j s_j \tag{10}$$

where m_j stands for the modal mass. On the other hand, because of orthogonality conditions, modes satisfy $\boldsymbol{\Psi}_j^{T,M}\mathrm{A}\boldsymbol{\Psi}_k^M = 0$ for any mode $j \neq k$, from which it can be derived that $\boldsymbol{\phi}_j^{T,M}\mathrm{C}\boldsymbol{\phi}_k^M = -(s_j + s_k)\boldsymbol{\phi}_j^{T,M}\mathrm{M}\boldsymbol{\phi}_k^M$. Considering that the eigenvalues appear as pairs of complex conjugates ($s_k = \bar{s_j}$), and taking into account that $\omega_j = |s_j|$ and $\zeta_j = -\mathrm{Re}[s_j]/|s_j|$, the precedent expression can be rewritten accordingly:

$$\boldsymbol{\phi}_j^{T,M}\mathrm{C}\bar{\boldsymbol{\phi}}_j^M = 2m_j\zeta_j\omega_j \tag{11}$$

Eq. (11) is used to approximate the term $\boldsymbol{\phi}_j^{T,M}\mathrm{C}\boldsymbol{\phi}_j^M$ in Eq. (10) by assuming that $\boldsymbol{\phi}_j^{T,M}\mathrm{C}\bar{\boldsymbol{\phi}}_j^M \approx \boldsymbol{\phi}_j^{T,M}\mathrm{C}\boldsymbol{\phi}_j^M$. In this way, noting that the modal mass is equal to 1 due to the normalisation to the mass matrix, Eq. (10) results into:

$$\boldsymbol{\Psi}_j^{T,M}\mathrm{A}\boldsymbol{\Psi}_j^M = 2m_j\zeta_j\omega_j + 2m_j s_j = 2(\omega_j\zeta_j + s_j) = \delta_j \tag{12}$$

where δ_j is the scaling parameter that allows to adapt the normalisation of the mode shapes from M to A:

$$\boldsymbol{\Psi}_j = \boldsymbol{\Psi}_j^M / \sqrt{\delta_j} \tag{13}$$

In a similar way, the modes comply with $\boldsymbol{\Psi}_j^{T,M}\mathrm{B}\boldsymbol{\Psi}_k^M = 0$ because of orthogonality conditions. This leads to $\boldsymbol{\phi}_j^{T,M}\mathrm{K}\bar{\boldsymbol{\phi}}_j^M \approx \boldsymbol{\phi}_j^{T,M}\mathrm{K}\boldsymbol{\phi}_j^M \approx \omega_j^2$ considering the previous approach. Then, further developing the expression $\boldsymbol{\Psi}_j^T\mathrm{B}\boldsymbol{\Psi}_j = \alpha_j$ while scaling as indicated in Eq. (13) allows to calculate the parameter α_j:

$$\alpha_j = \frac{(\omega_j^2 - s_j^2)}{\delta_j} \tag{14}$$

which can be used in Eq. (8) to solve the dynamic problem. Eventually, all the bridge modes are normalised according to this procedure and used to compute the solution as per Eq. (9), accounting for the modal contributions included in Table 3.

4.3. Quasi-static and dynamic loads

In this work, train induced vibrations are considered to be caused by three excitation mechanisms: a quasi-static contribution, a parametric excitation and a dynamic loading. The quasi-static contribution is modelled as a series of moving forces travelling at a constant speed and is related to the train axle load. In this approach, the inertial effects of the vehicle are neglected. On the other hand, the parametric excitation is induced by the moving loads circulating along rails discretely supported at each sleeper. Lastly, the dynamic loading includes the effect of track irregularities, which are modelled based on a stationary Gaussian random process characterised by its one-sided power spectral density (PSD) function $S(\kappa_x)$. Following the spectral representation theorem, samples of the unevenness profile $r(x)$ are generated as a superposition of harmonic functions with aleatory phase angles [45,46]:

$$r(x) = \sum_{n=1}^{Np} \sqrt{2\,S(\kappa_{xn})\Delta\kappa x}\cos(\kappa_{xn}x - \varphi_n) \tag{15}$$

where N_p is the number of points where the unevenness is calculated, κ_x is the sampling wavenumber, $\Delta\kappa_x$ is the wavenumber step and φ_n are the random phase angles uniformly distributed in the interval [0, 2π]. The artificial track irregularity profile is calculated from the PSD function below, in accordance with ISO 8608 standard [47]:

$$S(\kappa_x) = S(\kappa_{x0})\left(\frac{\kappa_x}{\kappa_{x0}}\right)^{-w} \tag{16}$$

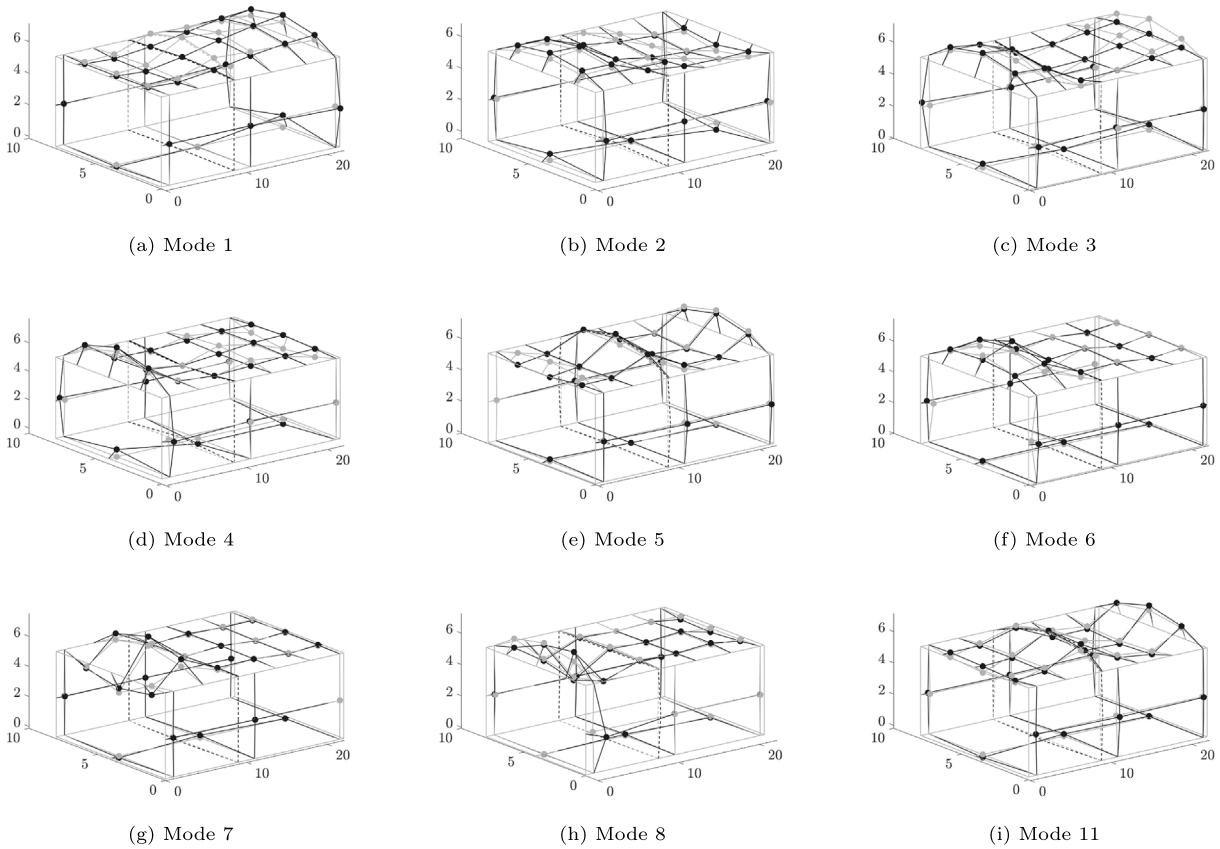

(a) Mode 1 (b) Mode 2 (c) Mode 3

(d) Mode 4 (e) Mode 5 (f) Mode 6

(g) Mode 7 (h) Mode 8 (i) Mode 11

Fig. 11. Comparison of the experimental (black) and numerical (gray) mode shapes. Modes 9 and 10 have not any numerical counterpart. (For interpretation of the references to colour in this figure legend, the reader is referred to the web version of this article.)

Table 4
Data about the train crossings simulated in the dynamic analyses.

Train	Track	Ride	Scheme	V [km/h]	d [m]	P [kN]
S599	1	CR–B	L-C-L	135.0	25.2	131
S100	2	M–S	L-8 C-L	235.4	18.70	156
S102 - Duplex	2	M–S	L-12 C-L//L-12 C-L	238.4	13.14	165
S114 - Duplex	3	S–M	L-2 C-L//L-2 C-L	236.5	25.90	153
S103	3	S–M	L-8 C-L	228.3	24.78	144

with $\kappa_{x0} = 1\text{rad/m}$. The exponent is set to $w = 3.5$, as commonly accepted for current HS lines [6]. The sampling wavenumber κ_x is defined in steps of $\Delta\kappa_x = \pi/V\,\text{rad/m}$ in the interval between the bogie passing frequency of each train divided by its travelling speed ($f_{pb}/V \cdot 2\pi = 2\pi/d$, where d is the characteristic distance of the train) and the ratio between the highest frequency of the bridge and the train velocity ($f_{11} \cdot 2\pi/V$). With respect to $S(\kappa_{x0})$, a range between 1×10^{-9} and 5×10^{-7} m^3 of PSD reference values for the rail unevenness is considered [48]. The lower bound describes a minor degree of irregularity and is applicable to rails in a good state of conservation. On the contrary, the upper bound involves a rougher unevenness of rails maintained in worse conditions. A value of $S(\kappa_{x0}) = 1 \times 10^{-9}$ m^3 is adopted for the HS tracks. In the conventional track, a slightly higher degree of deterioration is considered with $S(\kappa_{x0}) = 4 \times 10^{-8}$ m^3. This value is used for two main reasons: first, assuming a different level of maintenance compared to the HS line; and second, in accordance to more demanding traffic conditions in terms of loading, that include the circulation of heavy freight trains, which is generally excluded from the HS lines in the Spanish network [49]. In this regard, Fig. 12 shows the theoretical PSD function derived from Eq. (16) for tracks 1, 2, and 3.

Next, the irregularity profile is used to approximate the vehicle–track interaction force $F_{v/t}$ as a result of the track unevenness, as shown in Eq. (17):

$$F_{v/t}(x,\omega) = m_w \cdot \frac{d^2 r(x)}{dt^2} + Z^t_{d,z}(\omega) \cdot r(x) \tag{17}$$

where m_w is the vehicle unsprung mass and $Z^t_{d,z}(\omega)$ is the track vertical dynamic stiffness. This parameter is estimated from a harmonic analysis performed using the full track–bridge–soil interaction model. It considers two identical concentrated forces, $F_{z1}(\omega)$ and $F_{z2}(\omega)$, at midspan. Each load acts on one rail of the track. Then, the rail displacements in the points where the forces are being applied are obtained as $U_{z1}(\omega)$ and $U_{z2}(\omega)$. Finally, the track dynamic stiffness is computed:

$$Z^t_{d,z}(\omega) = \frac{1}{2}\left(\frac{F_{z1}(\omega) + F_{z2}(\omega)}{U_{z1}(\omega) + U_{z2}(\omega)}\right) \tag{18}$$

In a first approach, it is considered that the value of $Z^t_{d,z}$ at midspan is representative for the totality of the track length. In an analogous way to the calibration of the spring-dampers (see Section 3.3), $Z^t_{d,z}$ is admitted constant and equal to the value achieved at f_1.

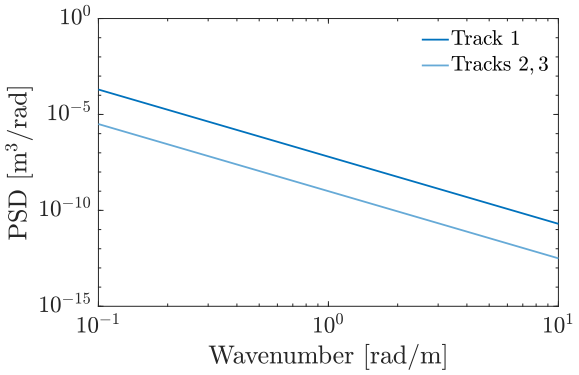

Fig. 12. Theoretical PSD functions associated to the irregularity profile of each track.

Table 5
Frequencies of the passenger coaches.

Train	S599	S100	S102	S114	S103	Unit
f_{v1}	0.79	1.15	1.07	0.78	0.79	Hz
f_{v2}	5.32	5.53	4.97	5.12	5.60	Hz

Table 6
Additional damping ratios to be considered for each train passage.

Train	S599	S100	S102	S114	S103	Unit
ζ_b	1.84	1.84	1.84	1.84	1.84	%
$\Delta\zeta_{\text{EADA}}$	0.36	0.42	0.24	0.31	0.93	%
ζ_{tot}	2.20	2.26	2.08	2.15	2.77	%

4.4. Additional damping

In the current setup, VBI effects are not considered. In this situation, where the vehicle is not explicitly simulated, the energy dissipated in its suspension systems is disregarded, potentially resulting in an overestimation of the bridge response [35,50]. To obtain a more realistic prediction of the structural performance, the VBI benefit may be approximated if an additional amount of damping ζ_{tot} is introduced in the system. In this work, this quantity is determined as follows:

$$\zeta_{\text{tot}} = \zeta_b + \Delta\zeta_{\text{EADA}} \tag{19}$$

where ζ_b is the structural damping of the bridge and $\Delta\zeta_{\text{EADA}}$ is the supplementary damping ratio proposed by Yau et al. [51] referred to as the Equivalent Additional Damping Approach (EADA). The first term of the precedent expression is obtained based on the EC [28] criterion for prestressed concrete bridges and, as shown in Eq. (20), depends solely on the span length L. The reason for not using the experimental damping for this purpose instead is because it was estimated with the bridge–soil system acting as a whole. In contrast, the simplified model adopts a decoupled approach, in which part of this damping effect is being already introduced by the spring-dampers in a direct way. Therefore, in terms of energy absorption, adopting the experimental damping (which is quite high in the lowest modes) as the total bridge contribution could result in an excessively non-conservative assumption.

$$\zeta_b = 1 + 0.07(20 - L) \tag{20}$$

On the other hand, $\Delta\zeta_{\text{EADA}}$ incorporates three ratios associated with the train–bridge modal properties that play an important role in the reduction of the bridge dynamic response due to the presence of the vehicle [50,52,53], as indicated in Eq. (21):

$$\Delta\zeta_{\text{EADA}} = \mu_1 r_1 \left|\frac{r_1 + 2\xi_{v1} i}{(1 - r_1{}^2) - 2\xi_{v1} i}\right| \tag{21}$$

where r_1 is the ratio between the fundamental vertical frequency of the passenger coaches and the first bending frequency of the bridge, μ_1 is

Fig. 13. Axles scheme of the trains CAF S599, Alstom S100, Talgo S102, Alstom S114 and Siemens S103.

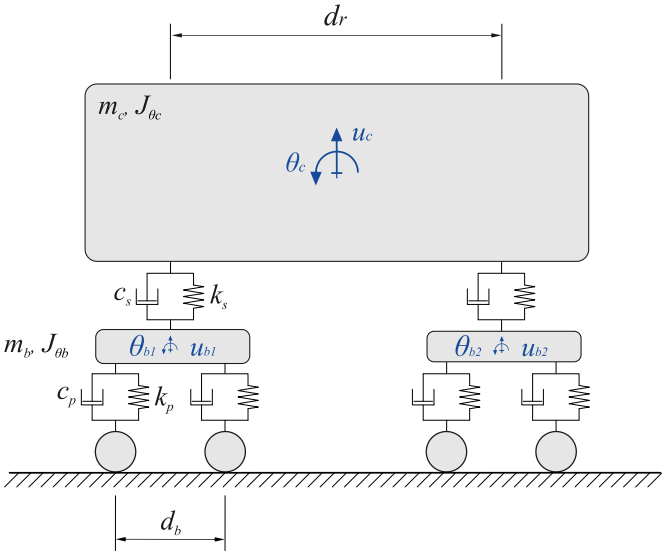

Fig. 14. Elements of the multi-body carriage model.

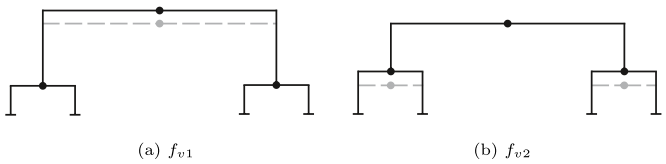

Fig. 15. Vertical mode shapes of the passenger coaches.

the corresponding vehicle–bridge modal mass ratio and ξ_{v1} is the effective suspension damping ratio. Eventually, ζ_{tot} is introduced in the system through each eigenvalue (s_j) under consideration, leading to the subsequent modified eigenvalues s_{jd} as indicated in Eq. (22). Then, the dynamic load problem is solved as previously explained.

$$s_{jd} = -(\zeta_j + \zeta_{\text{tot}})|s_j| + \text{Im}[s_j]i \tag{22}$$

5. Validation

In this section, the simplified model is used to predict the bridge dynamic response under operating conditions, and the results are validated with the experimental measurements. The data recorded in this regard correspond to the Renfe commercial passenger trains of the series S599, S100, S102, S114 and S103. Table 4 includes the subsequent information about these passages: train type, track number, travelling direction (CR: Ciudad Real, B: Badajoz, M: Madrid, S: Sevilla), coaches arrangement (L: locomotive, C: carriage), circulating speed V, characteristic distance d and mean axle load of the passenger coaches P_k.

Only one recording was available from a train travelling on track 1. This corresponds to the S599, a conventional train consisting of a central carriage and two external power cars. The distance between non-consecutive bogies of the middle car and a power car is $d = 25.2$ m. It also represents the single recording of a train travelling at conventional speed ($V = 135$ km/h). The rest of the trains circulated on tracks 2 and 3 and offered HS services. Among them, the S100 is an articulated train with eight carriages and two locomotives. The distance between shared bogies in the central carriages is $d = 18.7$ m. The S102 is a regular train and circulated with two power cars and twelve carriages in its duplex configuration. The distance between shared axles is $d = 13.14$ m. Next, the S114 is a conventional train composed of two integrated driver–passenger cars at both ends and two central coaches. This train presents a characteristic length of $d = 25.9$ m and ran in duplex configuration. Lastly, the conventional train S103 presents eight coaches and two integrated driver–passenger cars. The characteristic length between non-consecutive bogies in the central coaches is d = 24.775 m. Fig. 13 shows images of the trains and their scheme of axles. More information about these trains can be found in References [25,54].

5.1. Estimation of the additional damping

As mentioned in previous Section 4.4, an additional amount of damping ζ_{tot} is introduced to represent the effect of VBI in the system. Following Eq. (20), the structural damping according to EC [28] is calculated as $\zeta_b = 1.84$ % in the case of the portal frame under study. Then, the equivalent damping $\Delta\zeta_{\mathrm{EADA}}$[51] is computed as per Eq. (21). To obtain the modal properties of the trains, a 2D multi-body half-coach model is implemented using the FE method. This model includes the mass and inertia of the car body (m_c, I_{cy}) and the bogies (m_b, I_{by}); as well as the stiffness and damping of the primary (k_p, c_p) and secondary suspensions (k_s, c_s). As shown in Fig. 14, the model has a total of 6 DOFs that correspond to the vertical displacement of the car body z_c, the two bogies (z_{b1}, z_{b2}) and the rotation about the transverse axis of these same elements (θ_c and θ_{b1}, θ_{b2}, respectively). The suspension systems are represented as sets of parallel linear elastic spring-dampers. The model is calibrated with the properties of a central carriage of the train in question. The values provided in Reference [55] are adopted for the trains considered in the moving load problem.

After a performing a modal analysis, the vertical mode shapes of the vehicle shown in Fig. 15 are obtained. The first one is more associated to the properties of the secondary suspensions and comprises the upright displacement of the car body. Instead, the second one involves the movement of the bogies, as it depends on the characteristics of the primary suspensions. These mode shapes are identified for all the trains considered with the frequencies listed in Table 5.

The corresponding properties of the second vehicle mode f_{v2} are used to calculate the equivalent damping $\Delta\zeta_{\mathrm{EADA}}$. The basis for this is explained as it implies that the interaction between the bridge and the train is more significant when compared to f_{v1}, resulting into a greater equivalent damping ratio. However, given that $\Delta\zeta_{\mathrm{EADA}}$ serves a smaller complementary role in relation to the bridge damping ζ_b, the previous assumption still ensures that the approach remains within conservative bounds. Then, following Eq. (19), the total additional damping ζ_{tot} is obtained. Table 6 lists the results of all the trains.

5.2. Response under operating conditions

In what follows, the bridge dynamic response under passing trains is calculated and compared to experimental data. Both responses are filtered by applying Chebyshev filters with high-pass and low-pass frequencies of 1 and 30 Hz, respectively. The experimental acceleration is extracted from different sensors, selected based on the specific track the train is operating on: A4 in the case of the train running on track 1, A10 if it circulated on track 2, and A15 if track 3 was the case. First, time-history and RMS acceleration responses of every train passage are shown in Fig. 16. In this set of graphs, the experimental trace is depicted in black. The case including the quasi-static contribution is represented in blue and denoted as Q, whereas the one corresponding to the dynamic excitation in the form of rail irregularities is shown in red and denoted as I. On the other hand, the numerical response incorporating the quasi-static and the dynamic excitations (Q + I) is depicted in magenta. Lastly, the case including the previous excitations and the additional damping (Q + I + ζ_{tot}) is shown in light magenta.

As can be observed in Fig. 16, it is evident that the sole contribution of the quasi-static response is insufficient to capture the full dynamic behaviour of the bridge. This result is noticeable in both the time-histories and the RMS acceleration responses. Conversely, the case considering just the dynamic excitation exceeds the experimental results, even more when combined with the quasi-static contribution. This illustrates the importance of simulating this excitation mechanism, as previous research has identified track irregularities as a key factor contributing to increment the bridge response, mainly in terms of acceleration [56–58]. Apart from that, as clearly shown in the RMS plots, the additional damping is useful to adjust the previous outcome, dissipating further energy from the system and lowering the overall vibration intensity of the structure. This leads to a more accurate prediction when this effect is taken into account. These results are consistent across all the trains considered, obtaining more divergences in train S599, which circulated in track 1 in the conventional section.

Subsequently, the computed bridge response is examined in the frequency domain using the Fast Fourier Transform (FFT), the PSD, and one-third octave bands in the first, second, and third columns of Fig. 17, respectively. In this regard, from a broader point of view, the results obtained are in accordance with previous observations, highlighting that the contribution of the dynamic excitation is fundamental to achieve a good approximation to the experimental measurements. In a different vein, focusing on the analysis of the frequency content based on the FFT, the results present small peaks at lower frequencies, that are related to the characteristic distance of the train and subsequent harmonics. Then, the most prominent peaks occur near the structural modes of the bridge f_1–f_3 (i.e, between 22.4 and 26.8 Hz). The effect of the additional damping is more pronounced in these resonant peaks, reducing the amplitude of the response. Following, the PSD plots show that the vibrating energy of the bridge is mostly concentrated at frequencies higher than $20Hz$, presenting various minor peaks below this threshold. As probably due to the decoupling of the two bridge sections, the PSD plot of train S599 in Fig. 17(b) shows a negligible contribution of the fundamental mode of the HS section ($f_1 = 22.4$ Hz). Similarly, for trains running on track 2 in the HS section (see Fig. 17(e, h)), the response exhibits little contribution from the fundamental mode of the conventional zone ($f_3 = 26.8$ Hz). Nevertheless, the response of the passages from track 3 (see Fig. 17(k, n))) depicts a higher participation of this mode, which may also be influenced by the proximity of $f_2 = 25.4$ Hz, a mode involving the longitudinal bending of the two bridge sections. In relation to the one-third octave band spectrum, these plots are computed according to the German standard DIN 45672-2 [59] on a reference period during which the response is considered stationary. The results in this regard show that the bridge behaviour is dominated by high-frequency bands (i.e., > 16 Hz), where the contribution of the dynamic excitation is higher, and the bridge frequencies appear.

If the results are evaluated depending on the train type, it is observed that greater divergences are found in the train S599, which circulated on track 1 (see Fig. 17(a–c)). This may be attributable to a higher uncertainty about the track conditions (in relation to the degree of unevenness) favoured by a lack of data of more trains running on this track to perform further investigations in this regard. It is also important to note that the irregularity profile is estimated based on a numerical approach. Thus, despite the results in the other tracks suggesting a good approximation, the real profile may differ from the projected one. Another factor affecting the predicted acceleration in track 1 may be related to the size of the conventional section and the proximity to the longitudinal joint. From that perspective, given that this section has a reduced area if compared to the HS zone, the relative influence of the joint could be more significant. Therefore, the modal behaviour of this part of the bridge could be subjected to more variability, leading to more deviations in the predicted response. On the contrary, the results from track 2 and, especially, from track 3, provide good predictions of the experimental results. The small deviations detected among the train passages on track 2 (see Fig. 17(d–i)) may be prompted by the proximity to the longitudinal joint, as these divergences attenuate in the trains from track 3 (see Fig. 17(j–o)), which is the farthest from this element.

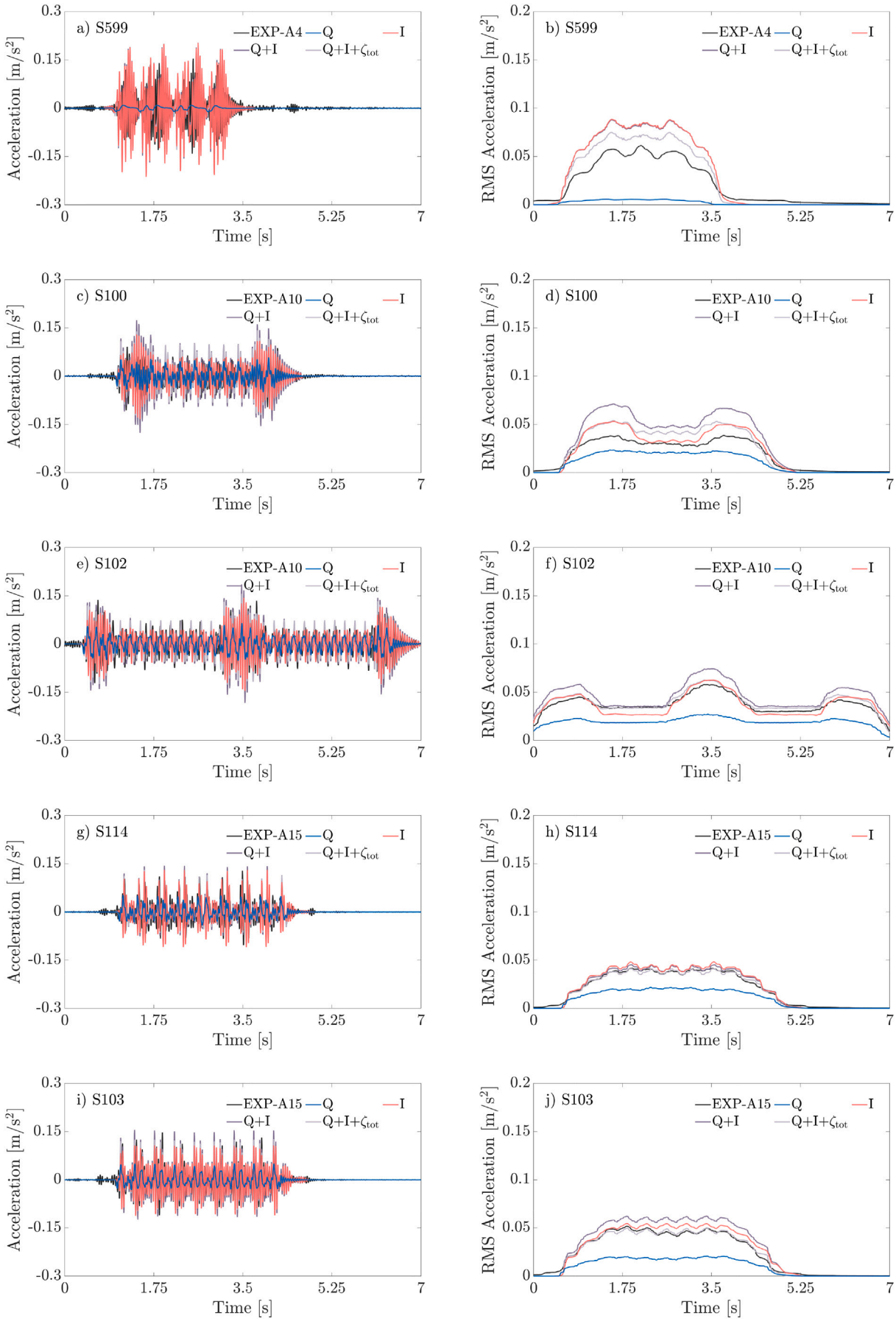

Fig. 16. Comparison of the experimental and numerical responses: time-history and RMS acceleration of each train passage.

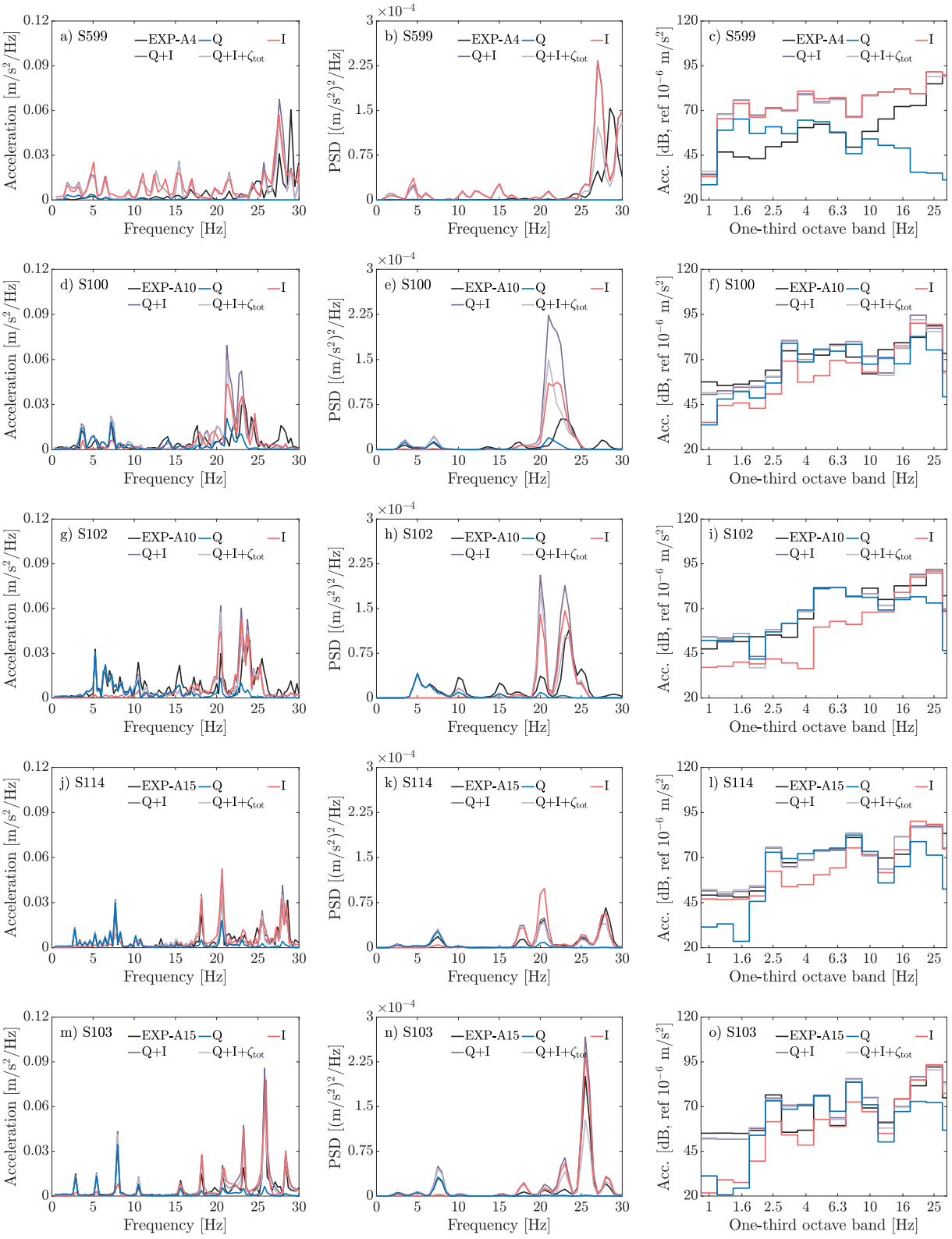

Fig. 17. Comparison of the experimental and computed responses: FFT, PSD, and one-third octave bands.

6. Conclusions

In this contribution, a procedure to efficiently simulate the effect of SSI on railway bridges is proposed. In order to assess its suitability, the procedure is applied to the case of an existing portal frame railway bridge. In this regard, a complete study is provided, starting from the acquisition of experimental data and the identification of its modal parameters. Then, a full track–bridge–soil interaction model including an explicit idealisation of the soil domain is implemented to simulate SSI in a detailed manner and obtain dynamic stiffness functions

representing the coupled bridge–soil behaviour. Then, a simplified version of this model is implemented, but in this case, the soil is substituted by a series of linear spring-damper elements, that are calibrated based on the properties of stiffness and damping derived from the previous dynamic functions. Subsequently, the moving load problem is addressed and solved by means of CMS. To obtain a more realistic prediction of the bridge response under passing trains, track irregularities are included in the analyses. Moreover, as the vehicle is not explicitly simulated, the bridge damping is increased to account for the effect of VBI by means of the EADA method. Finally, the performance of the portal frame under operating conditions is calculated with the primary aim of validating the proposed approach, and, additionally, evaluating the dynamic response of the bridge and the main factors affecting it. In this way, the conclusions of the work can be summarised as follows:

- The proposed numerical approach has been satisfactorily implemented and validated in the case of a portal frame railway bridge using 3D FE formulations. By incorporating a reduced-order model with dynamic stiffness functions representing the SSI effect, the dynamic moving load problem is solved efficiently without incurring excessive computational cost. In general, the results obtained replicate the experimental bridge response with an acceptable degree of accuracy. For this reason, this approach could be useful to simulate SSI in other portal frames or semi-buried structures, as well as in different bridge configurations. Besides, the approach to adapt the normalisation of the mode shapes in an approximated manner could be of utility for other cases.
- In relation to the particular case study, given that this bridge is divided into two coupled structures by a longitudinal joint, the initial process of acquisition of experimental data and the posterior modal identification were key to understand its complex modal behaviour and to adapt the numerical model to the real conditions of the structure. In relation to this, it was fundamental to differentiate the mechanical properties of the conventional and the HS sections.
- From the experimental–numerical comparison of the bridge under operating conditions, it can be derived that taking into account the dynamic excitation is essential to achieve a good approximation of the experimental response. In this regard, the analysis of the results reveals that the bridge response is mainly influenced by frequencies higher than 15 Hz, where the track irregularities have the most noticeable impact and the first three bridge modes appear. Comparing the results train by train, more divergences between the experimental and the numerical responses are found in the case of those circulating on track 1, and better results are achieved in tracks 2 and 3. In this context, differences between trains running on different tracks point to an apparent disparity increment in the cases where the influence of the joint is likely higher. This is particularly evident in track 1, where its proximity to this element, combined with its location within the conventional section, may increase the impact of the joint on the modal behaviour of this part of the bridge, adding complexity and making it more complicated to predict. Similarly, regarding trains running on track 2, it is probable that the small deviations detected in frequencies far from structural modes may be boosted by the proximity of this track to the joint, as these divergences attenuate in the trains from track 3, which is the farthest from this element. Still, the predictions are reasonably accurate in both cases.
- Overall, the attenuating effect introduced by means of the additional damping with the EADA method has been practical to provide a more accurate prediction of the bridge response under operating conditions. The impact of this phenomenon is more pronounced at resonance, making it a suitable approach for simulating the influence of VBI when using moving-load models.

In brief, this investigation explores the application of a substructuring approach to model SSI on railway bridges, aiming to reduce the typically high computational cost associated with simulating this interaction mechanism. The results show that this procedure could be of utility to assess the performance of existing structures and for designing new bridges. Future works could implement additional refinements on the proposed approach, such as, for example, explicitly introducing VBI effects to avoid overestimating the bridge response or a more detailed definition of the soil strata. Overall, this work contributes to improving the predictive capabilities on railway bridge dynamics while considering SSI, thereby enhancing safer, more sustainable, and cost-effective infrastructure.

CRediT authorship contribution statement

J. Chordà-Monsonís: Writing – review & editing, Writing – original draft, Visualization, Validation, Software, Methodology, Investigation, Formal analysis, Conceptualization. **J.C. Sánchez-Quesada:** Software, Investigation, Formal analysis, Conceptualization. **E. Moliner:** Writing – original draft, Validation, Supervision, Software, Methodology, Investigation, Funding acquisition, Formal analysis, Conceptualization. **A. Romero:** Writing – review & editing, Writing – original draft, Supervision, Funding acquisition, Conceptualization. **P. Galvín:** Writing – review & editing, Writing – original draft, Validation, Supervision, Software, Methodology, Investigation, Funding acquisition, Formal analysis, Conceptualization. **M.D. Martínez-Rodrigo:** Writing – review & editing, Writing – original draft, Validation, Supervision, Software, Methodology, Investigation, Funding acquisition, Formal analysis, Conceptualization.

Declaration of competing interest

The authors declare that they have no known competing financial interests or personal relationships that could have appeared to influence the work reported in this paper.

Acknowledgements

The authors acknowledge the following institutions for their financial support: Universitat Jaume I through the contract (PREDOC/2022/26) and the grant (E-2023-08); Spanish Ministry of Science and Innovation, Agencia Española de la Investigación (AEI) and FEDER EU Funds (PID2022-138674OB-C2); Regional Government of Economic Transformation, Industry, Knowledge and Universities of Andalusia (PROYEXCEL00659); and the Andalusian Scientific Computing Centre (CICA).

This project has received funding from the Europe's Rail Joint Undertaking under Horizon Europe research and innovation programme under grant agreement No. 101121765 (HORIZON-ER-JU-2022-ExplR-02). Views and opinions expressed are however those of the author(s) only and do not necessarily reflect those of the European Union or Europe's Rail Joint Undertaking. Neither the European Union nor the granting authority can be held responsible for them.

References

[1] Zangeneh A, François S, Lombaert G, Pacoste C. Modal analysis of coupled soil-structure systems. Soil Dyn Earthq Eng 2021;144:106645.
[2] Zangeneh A, Svedholm C, Andersson A, Pacoste C, Karoumi R. Identification of soil-structure interaction effect in a portal frame railway bridge through full-scale dynamic testing. Eng Struct 2018;159:299–309.
[3] Salcher P, Onay A, Adam C. Effekt DER Boden-bauwerksinteraktion auf die dynamik rahmenartiger eisenbahnbrücken (effect of soil-structure interaction on the dynamics of portal frame railway bridges. Bautechnik 2020;97(7):490–8.
[4] Galvín P, Romero A, Moliner E, Connolly DP, Martínez-Rodrigo MD. Fast simulation of railway bridge dynamics accounting for soil–structure interaction. Bull Earthq Eng 2022;20(7):3195–213.
[5] Östlund JL, Andersson A, Ülker Kaustell M, Battini J. On the influence of shallow soil strata on the dynamic soil–structure interaction of simply supported high-speed railwaybridges. Int J Rail Transp 2021;9(5):405–23.
[6] Romero A, Solís M, Domínguez J, Galvín P. Soil-structure interaction in resonant railway bridges. Soil Dyn Earthq Eng 2013;47:108–16.
[7] Báez M, Fraile A, Fernández J, Hermanns L. A vibration prediction model for culvert-type railroad underpasses. Eng Struct 2018;172:1025–41.

[8] Heiland T, Hendrawan D, Wuttke F, Stempniewski L, Stark A. Influence of soil-structure interaction on the dynamic characteristics of railroad frame bridges. Soil Dyn Earthq Eng 2023;167:107800.
[9] Zangeneh A, Battini JM, Pacoste C, Karoumi R. Fundamental modal properties of simply supported railway bridges considering soil-structure interaction effects. Soil Dyn Earthq Eng 2019;121:212–8.
[10] Martínez-Rodrigo MD, Galvín P, Doménech A, Romero A. Effect of soil properties on the dynamic response of simply-supportedbridges under railway traffic through coupled boundary element-finite element analyses. Eng Struct 2018;170:78–90.
[11] Romero A, Galvín P. A BEM–FEM using layered half-space green's function in time domain for ssi analyses. Eng Anal Bound Elem 2015;55:93–103.
[12] Tehrani SAH, Andersson A, Zanganeh A, Battini J. Dynamic soil–structure interaction of a three-span railway bridge subject tohigh-speed train passage. Eng Struct 2024;301:117296.
[13] Reumers P, Lombaert G, Degrande G. The effect of foundation–soil–foundation interaction on the response of continuous, multi-span railway bridges. Eng Struct 2024;299:117096.
[14] Galvín P, Domínguez J. High-speed train-induced ground motion and interaction with structures. J Sound Vib 2007;307(3–5):755–77.
[15] Vega J, Fraile A, Alarcón E, Hermanns L. Dynamic response of underpasses for high-speed train lines. J Sound Vib 2012;331(23):5125–40.
[16] Ülker Kaustell M, Karoumi R, Pacoste C. Simplified analysis of the dynamic soil–structure interaction of a portal frame railway bridge. Eng Struct 2010;32(11):3692–8.
[17] Heiland T, Stempniewski L, Stark A. The dynamic characteristics of railway portal frame bridges: a comparison between measurements and calculations. Appl Sci 2024;14(4):1493.
[18] Sandqvist N, Milicevic M. Soil-structure interaction analysis of portal frame railway bridges, [Master thesis]. Stockholm, Sweden: KTH Royal Institute of Technology, School of Architecture and the Built Environment, SE-100 44, 2020.
[19] Ikzer R. Dynamic soil-structure interaction of a portal frame railway bridge-numerical analysis on a case study bridge, [Master thesis]. Stockholm, Sweden: KTH Royal Institute of Technology, School of Architecture and the Built Environment, SE-100 44, 2018.
[20] Dagdelen T, Ruhani S. Finite element analysis of the dynamic effect of soil-structure interaction of portal frame bridges-a parametric study, [Master thesis]. Stockholm, Sweden: KTH Royal Institute of Technology, School of Architecture and the Built Environment, SE-100 44, 2018.
[21] Tehrani SAH, Zangeneh A, Andersson A, Battini JM. Simplified soil–structure interaction modeling techniques for the dynamic assessment of end shield bridges. Eng Struct 2024;319:118803.
[22] Google Earth. Camino de las huertas underpass, argamasilla de calatrava, 38°45'09"n 4°04'50"w [online]. 2020. Available from https://www.google.es/intl/es/earth/index.html [Accessed 22 Oct 2024].
[23] International Organization for Standardization ISO 2631-2: 1999, mechanical vibration and shock-evaluation of human exposure to whole-body vibration - part 2: vibration in buildings (1–80 Hz); 1999.
[24] Zahid FB, Ong ZC, Khoo SY. A review of operational modal analysis techniques for in-service modal identification. J Braz Soc Mech Sci Eng 2020;42(398).
[25] Galvín P, Romero A, Moliner E, De Roeck G, Martínez-Rodrigo MD. On the dynamic characterisation of railway bridges through experimental testing. Eng Struct 2021;226:111261.
[26] Cheynet E. Damping ratio estimation from ambient vibrations (SDOF). 2020. https://zenodo.org/record/3827107.
[27] Ibrahim SR. Random decrement techniquefor modal identification of structures. J Spacecraft 1977;14(11):696–700.
[28] CEN, EN 1991-2. Eurocode 1: actions on structures-part 2: traffic loads on bridges and other civil engineering works. European Committee for Standardization (CEN), Brussels; 2023.
[29] Coronado C, Gidwani N. Calculation of dynamic impedance foundations using finite element procedures, San Francisco: Bechtel Power Corporation Nuclear Security and Environmental Edition 2016.
[30] Ministerio de Fomento, Gobierno de España. IF3-instrucción para el proyecto y construcción de obras ferroviarias. 2015.
[31] Ministerio de Transportes. Turismo y comunicaciones, nuevo acceso ferroviario a andalucía: proyecto de infraestructura y vía del tramo ciudad real-brazatortas. Documento n.1, memoria y anejos. INECO; 1987 VI.
[32] Ministerio de Transportes. Turismo y comunicaciones, nuevo acceso ferroviario a andalucía: proyecto de infraestructura y vía del tramo ciudad real-brazatortas, documento n.1, memoria y anejos. INECO; 1987 III.
[33] Doménech A, Martínez-Rodrigo MD, Romero A, Galvín P. On the basic phenomenon of soil–structure interaction on the free vibration response of beams: application to railway bridges. Eng Struct 2016;125:254–65.
[34] CEN/TC256. EN 13674-1:2011 + a1:2017 railway applications-track-rail-part 1: Vignole railway rails 46 kg/m and above. Brussels: European Committee for Standardization; 2017.
[35] Chordà-Monsonís J, Romero A, Moliner E, Galvín P, Martínez-Rodrigo MD. Ballast shear effects on the dynamic response of railway bridges. Eng Struct 2022;272:114957.
[36] Ministerio de Fomento. Gobierno de España, instrucción de acciones a considerar EN puentes de ferrocarril. 2010.
[37] NAV 3-1-3.1. Traviesas bibloque de hormigón. Administrador de infraestructuras ferroviarias (ADIF) 1a Edición: Septiembre de 1998.
[38] Zhai W, Wang K, Lin J. Modelling and experiment of railway ballast vibrations. J Sound Vib 2004;270(4–5):673–83.
[39] Liu K, Lombaert G, Roeck GD. Dynamic analysis of multispan viaducts with weak coupling between adjacent spans. J Bridge Eng 2014;19(1):83–90.
[40] Sánchez-Quesada JC, Moliner E, Romero A, Galvín P, Martínez-Rodrigo MD. Ballasted track interaction effects in railway bridges with simply-supported spans composed by adjacent twin single-track decks. Eng Struct 2021;247:113062.
[41] Malveiro J, Ribeiro D, Calçada R, Delgado R. Updating and validation of the dynamic model of a railway viaduct with precast deck. Struct Infrastruct Eng 2014;10(11):1484–509.
[42] Hurty W, Rubinstein M. Dynamics of structures. Hoboken: Prentice-Hall Inc; 1965.
[43] Shampine L, Reichelt M. The Matlab ODE suite. SIAM J Sci Comput 1997;18(1):1–22.
[44] Dormand J, Prince P. A family of embedded runge-kutta formulae. J Comput Appl Math 1980;6(1):19–26.
[45] Lombaert G, Degrande G. Ground-borne vibration due to static and dynamic axle loads of intercity and high-speed trains. J Sound Vib 2009;319(3–5):1036–66.
[46] Chordà-Monsonís J, Moliner E, Galvín P, Martínez-Rodrigo MD, Zacchei E, Tadeu A, Ferraz I, Romero A. Dynamic load allowance of long-span modular steel bridges. Eng Struct 2023;282:115835.
[47] International Organization for Standardization. ISO 8608: 2016, mechanical vibration-road surface profiles-reporting of measured data. 2016.
[48] Lombaert G, Degrande G, Kogut J, François S. The experimental validation of a numerical model for the prediction of railway induced vibrations. J Sound Vib 2006;297(3–5):512–35.
[49] Comisión Nacional de los Mercados y la Competencia. Informe anual del sector ferroviario (2023), Tech. rep., CNMC; 2024.
[50] Doménech A, Museros P, Martínez-Rodrigo MD. Influence of the vehicle model on the prediction of the maximum bending response of simply-supported bridges under high-speed railwaytraffic. Eng Struct 2014;72:123–39.
[51] Yau J, Martínez-Rodrigo MD, Doménech A. An additional damping approach to assess vehicle-bridge interaction for train-induced vibration of short-span railway bridges. Eng Struct 2019;188:469–79.
[52] Arvidsson T, Karoumi R, Pacoste C. Statistical screening of modelling alternatives in train–bridge interaction systems. Eng Struct 2014;59:693–701.
[53] Stoura CD, Dimitrakopoulos EG. Additional damping effect on bridges because of vehicle-bridge interaction. J Sound Vib 2020;476:115294.
[54] RENFE, Nuestros trenes, https://www.renfe.com/es/va/grup-renfe/grup-renfe/flota-de-trens [Accessed 2 Dec 2024].
[55] Sánchez-Quesada JC, Moliner E, Romero A, Galvín P, Martínez-Rodrigo MD. Train-track-bridge interaction effects on highly skewed girder bridges of short-to-medium spans for increasing operating speeds. Struct Infrastruct Eng 2024:1–25.
[56] Peixer M, Montenegro P, Carvalho H, Ribeiro D, Bittencourt T, Calçada R. Running safety evaluation of a train moving over a high-speed railway viaduct under different track conditions. Eng Fail Anal 2021;121:105133.
[57] Salcher P, Adam C, Kuisle A. A stochastic view on the effect of random rail irregularities on railway bridge vibrations. Struct Infrastruct Eng 2019;15(12):1649–64.
[58] Allahvirdizadeh R, Andersson A, Karoumi R. Reliability assessment of ballasted railway bridges considering soil-structure interaction using ensemble of surrogate models. Int J Rail Transp 2024;13(3):1–22.
[59] Deutsches Institut für normung, DIN 45672 teil 2-schwingungsmessungen in DER umgebung von schienenverkehrswegen: auswerteverfahren; 1995.